CrossMark

JFM PAPERS

Membrane flutter in three-dimensional inviscid flow

Christiana Mavroyiakoumou[1],† and Silas Alben[1],†

[1]Department of Mathematics, University of Michigan, Ann Arbor, MI 48109, USA

We develop a model and numerical method to study the large-amplitude flutter of rectangular membranes (of zero bending rigidity) that shed a trailing vortex-sheet wake in a three-dimensional (3-D) inviscid fluid flow. We apply small initial perturbations and track their decay or growth to large-amplitude steady-state motions. For 12 combinations of boundary conditions at the membrane edges we compute the stability thresholds and the subsequent large-amplitude dynamics across the three-parameter space of membrane mass density, pretension and stretching rigidity. With free side edges we find good agreement with previous 2-D results that used different discretization methods. We find that the 3-D dynamics in the 12 cases naturally forms four groups based on the conditions at the leading and trailing edges. The deflection amplitudes and oscillation frequencies have scalings similar to those in the 2-D case. The conditions at the side edges, although generally less important, may have small or large qualitative effects on the membrane dynamics – e.g. steady vs unsteady, periodic vs chaotic or the variety of spanwise curvature distributions – depending on the group and the physical parameter values.

Key words: flow–structure interactions, nonlinear instability

1. Introduction

Interactions between flexible structures and high-Reynolds-number flows are ubiquitous in nature and engineering applications. The physical mechanisms that govern these fluid–structure interactions provide us with important insights into the fluid dynamics of biolocomotion. For example, fish can exploit energy from surrounding vortices and move efficiently by undulating their bodies (Triantafyllou, Triantafyllou & Yue 2000; Gazzola, Argentina & Mahadevan 2014), or synchronize their motions with the oncoming vortices (Liao *et al.* 2003). These observations have inspired engineers to design and manufacture continuously deformable robots that exhibit these behaviours (Lauder *et al.* 2007; Rus

† Email addresses for correspondence: chrismav@umich.edu, alben@umich.edu

953 A32-1

& Tolley 2015; Li *et al.* 2017). Birds and other flying animals also take advantage of such mechanisms to achieve efficient locomotion. In particular, bats – one of nature's most agile fliers (Swartz *et al.* 1996; Shyy, Berg & Ljungqvist 1999; Swartz *et al.* 2007; Song *et al.* 2008; Cheney *et al.* 2015) – can adapt to the surrounding flow conditions by deforming their thin, compliant membrane wings.

An extensible membrane is a soft material that undergoes significant stretching in a fluid flow and has negligible bending rigidity. When it is aligned with a fluid flow, the surrounding fluid forces can cause it to flutter and become unstable. Being able to predict the onset of membrane instability across parameter space, either by flutter, divergence or a combination of the two, is fundamental to a wide range of applications. Stable membranes can be used in a variety of configurations in aircraft and shape-morphing airfoils (Abdulrahim, Garcia & Lind 2005; Lian & Shyy 2005; Hu, Tamai & Murphy 2008; Stanford *et al.* 2008; Jaworski & Gordnier 2012; Piquee *et al.* 2018; Schomberg *et al.* 2018; Tzezana & Breuer 2019), sails (Colgate 1996; Kimball 2009) parachutes (Pepper & Maydew 1971; Stein *et al.* 2000) and micro-air vehicles (Lian & Shyy 2005). When a rigid wing moves through a flow its upper surface may experience flow separation and significant reductions in aerodynamic efficiency in both steady and unsteady flows, thus limiting the aircraft's manoeuvrability and performance. However, a flexible membrane is able to adapt quickly to unsteady airflow conditions by assuming a deformed shape that can inhibit flow separation and enhance aircraft manoeuvrability. Recent developments in membrane aerodynamics are reviewed in Lian *et al.* (2003) and Tiomkin & Raveh (2021).

The regions in parameter space where membrane flutter occurs have been predicted by linear models that mostly assume an infinite membrane span and two-dimensional (2-D) flow. In this work we use a three-dimensional (3-D) inviscid flow model based on the vortex-lattice method to study membrane stability in the linear regime of small deflections as well as large-amplitude nonlinear membrane dynamics. We find qualitative changes in flutter behaviour in some cases due to three-dimensionality.

Only a small number of studies have considered fully coupled interactions of flexible bodies and 3-D inviscid flows. The formulation of the mechanical force balance laws and the numerical methods are more complicated in three dimensions than in two dimensions and the computational expense is much higher. Inviscid flow models such as the vortex-lattice method are widely used to model viscous high-Reynolds-number flows for aquatic and aerodynamic propulsion (Kagemoto *et al.* 2000; Katz & Plotkin 2001; Shukla & Eldredge 2007; Michelin & Llewellyn Smith 2009; Willis & Persson 2014; Ayancik, Mivehchi & Moored 2022) because the computational cost is generally much lower than for direct solvers (e.g. in the case of complex and deforming body geometries, immersed-boundary, lattice-Boltzmann and deforming-mesh methods (Kim & Peskin 2007; Willis *et al.* 2007*a*; Zhu *et al.* 2011; Hoover *et al.* 2021)). In the inviscid models computational elements are distributed along surfaces rather than throughout the flow volume. However, traditional inviscid approximations of flow separation work well only in certain cases such as low-angle-of-attack airfoils where trailing-edge separation is dominant. Recently leading-edge separation has been included in such models (Pan *et al.* 2012; Ramesh *et al.* 2014).

Several recent works have studied the effect of various dimensionless control parameters such as Reynolds number, density ratio, shear modulus and aspect ratio on the flutter of one or more thin plates or flags with bending rigidity in 3-D viscous, high-Reynolds-number flows (Huang & Sung 2010; Tian, Lu & Luo 2012; Yu, Wang & Shao 2012; Banerjee, Connell & Yue 2015; Dong, Chen & Shi 2016; Chen *et al.* 2020). Immersed-boundary methods were used by Tian *et al.* (2012) and Huang & Sung (2010). Yu *et al.* (2012) used

a fictitious domain method, and Banerjee *et al.* (2015) used a coordinate transformation method.

Immersed-boundary methods have also been used to study a number of 3-D swimming problems, such as the self-propulsion of flapping flexible plates (Masoud & Alexeev 2010; Tang *et al.* 2016), the role of active muscle contraction, passive body elasticity and fluid forces in forward swimming (Mittal *et al.* 2008; Borazjani *et al.* 2013; Hoover, Griffith & Miller 2017; Dawoodian & Sau 2021; Hoover *et al.* 2021) and the propulsive forces acting on flexible fish bodies (Hoover & Tytell 2020).

Boundary element methods have helped identify the effects of body kinematics on thrust production and efficiency of 3-D swimmers with non-deforming (Liu 1996; Liu & Bose 1997) and deforming wakes (Zhu *et al.* 2002). Moored (2018) used a boundary element method to examine the self-propelled swimming of undulatory fins and manta rays (Fish *et al.* 2016), and to derive 3-D heaving and pitching scaling laws (Ayancik, Fish & Moored 2020; Ayancik *et al.* 2022).

In the case of membranes with negligible bending stiffness, arbitrary Lagrangian–Eulerian methods have been used to study the role of leading-edge vortices in the flutter instability (Li, Jaiman & Khoo 2021) and large-amplitude dynamics, particularly at large angles of attack (Li, Law & Jaiman 2019; Li, Jaiman & Khoo 2022). Here, for simplicity, we focus on the zero-angle-of-attack case and neglect leading-edge separation.

There are relatively few studies of 3-D coupled interactions of inviscid flows and flexible bodies. Recently, Hiroaki, Hayashi & Watanabe (2021) and Hiroaki & Watanabe (2021*b*) used nonlinear beam theory and the vortex-lattice method to analyse the limit cycle oscillations of a rectangular plate and plate vibration under harmonic forced excitation (Hiroaki & Watanabe 2021*a*). Previously Gibbs, Wang & Dowell (2012, 2015) studied the 3-D linear stability problem for a flexible plate in an inviscid flow with various boundary conditions. Tang, Dowell & Hall (1999) and Tang & Dowell (2001) used the method to study the stability of delta wings and rectangular plates, and Murua, Palacios & Graham (2012) reviewed the vortex-lattice method in similar applications.

To our knowledge the present paper is the first 3-D study of the large-amplitude dynamics of membranes (of zero bending rigidity) in inviscid flows. Here, we use a flat-wake approximation (Kagemoto *et al.* 2000) and find good agreement between membranes with large aspect ratio in 3-D flow and membranes in 2-D flow with wake roll-up. Computing wake roll-up with high precision in three dimensions is challenging as the vortex sheet may undergo complex twisting and shearing deformations that make meshing difficult (Feng 2007). Fast algorithms (e.g. tree codes) for the evolution of vortex sheets in three dimensions have been developed by Kaganovskiy (2006), Feng, Kaganovskiy & Krasny (2009), Lindsay & Krasny (2001), Willis, Peraire & White (2007*b*) and Sakajo (2001).

In Mavroyiakoumou & Alben (2020) we studied the membrane dynamics in a 2-D flow, where the membrane is a 1-D curvilinear segment that undergoes large deflections. We first studied the most common endpoint conditions, 'fixed–fixed', in which the membrane ends were held fixed, as in most previous studies of membrane flutter (Le Maître, Huberson & De Cursi 1999; Sygulski 2007; Tiomkin & Raveh 2017; Nardini, Illingworth & Sandberg 2018). We found, surprisingly, that all unstable membranes tended to a steady shape in the large-amplitude regime, except for some cases with unrealistically large deflections. This motivated us to study a second case, 'fixed–free', in which the trailing edge of the membrane is free to move, but only in the direction perpendicular to the oncoming flow. This corresponds to the free-end boundary condition for a string or membrane in classical mechanics (Graff 1975; Farlow 1993), where the membrane end

has horizontal slope. Physically, this boundary condition means that the end slides without friction perpendicularly to the membrane's flat equilibrium state (for example, in Farlow (1993) the end is attached to a frictionless, massless ring). If the membrane end is also free to move in the in-plane direction, compression develops and the problem is ill posed without a stabilizing effect such as bending rigidity, and difficult to solve computationally (Triantafyllou & Howell 1994). Recent work has studied unsteady motions by membranes with partially free edges. In Hu *et al.* (2008), the authors study membrane wings with partially free trailing edges and find that trailing-edge flutter can occur when the angle of attack is relatively low. Arbós-Torrent, Ganapathisubramani & Palacios (2013) found experimentally that membrane wing flutter can be enhanced by the vibrations of flexible leading- and trailing-edge supports. Partially free edges exist also in sails with tensioned cables running along the edges (Kimball 2009). At sufficiently low tension these edges may flutter (Colgate 1996). A related application is to energy harvesting by membranes mounted on tensegrity structures (networks of rigid rods and elastic fibres) and placed in fluid flows (Sunny, Sultan & Kapania 2014; Yang & Sultan 2016). In such cases the membrane ends have some degrees of freedom akin to the free-end boundary conditions we have defined above. Recent studies have also considered interactions of flags (Mougel & Michelin 2020) and membranes (Labarbe & Kirillov 2020, 2022) with a free surface, including flutter behaviour.

The structure of the paper is as follows. Section 2 describes our large-amplitude membrane-vortex-sheet model. Unlike our previous work (Mavroyiakoumou & Alben 2020, 2021*b*,*a*), here, we consider a membrane surface held in a 3-D inviscid flow with 12 different sets of boundary conditions. We solve this nonlinear model using Broyden's method and an unsteady vortex-lattice algorithm. Section 3 describes the numerical method. We apply a small initial perturbation to the membrane in the direction transverse to the flow and compute the subsequent dynamics, which has large-amplitude deflections if the membrane is unstable. In § 4 we perform convergence studies and validate our model by comparing the current results with our previous 2-D studies of fixed–fixed, fixed–free and free–free membranes. Section 5 describes the computed membrane dynamics and how this varies with key parameters such as the membrane mass, pretension and stretching rigidity. We find that the membrane dynamics naturally forms four groups based on the boundary conditions at the leading and trailing edges. The 3-D dynamics differs from the 2-D dynamics in several ways: in the fixed–fixed case there are unsteady 3-D motions with varying degrees of up–down asymmetry; there are complex spanwise deformations in the 3-D free–free case and some other cases with free side edges; steady, periodic and chaotic motions appear at different parameter values, and very different midspan membrane profiles appear in three dimensions. Section 6 gives the conclusions.

2. Large-amplitude membrane-vortex-sheet model

We consider the motion of an extensible membrane held in a 3-D fluid flow with velocity $U\hat{e}_x$ in the far field (see figure 1). In the undeformed state the membrane is flat and parallel to the flow in the plane $z = 0$. As in Alben *et al.* (2019), the membrane obeys linear elasticity but undergoes large deflections, so geometrically nonlinear terms enter the force expression. The membrane has a small thickness h and to leading order the deformations do not vary through the thickness, so they can be described by the middle surface, midway through the thickness. The middle surface is a geometric surface, a three-component vector parametrized by two spatial coordinates and time, $\boldsymbol{r}(\alpha_1, \alpha_2, t) = (x(\alpha_1, \alpha_2, t), y(\alpha_1, \alpha_2, t), z(\alpha_1, \alpha_2, t)) \in \mathbb{R}^3$, where the spatial coordinates $\alpha_1 \in [-L, L]$
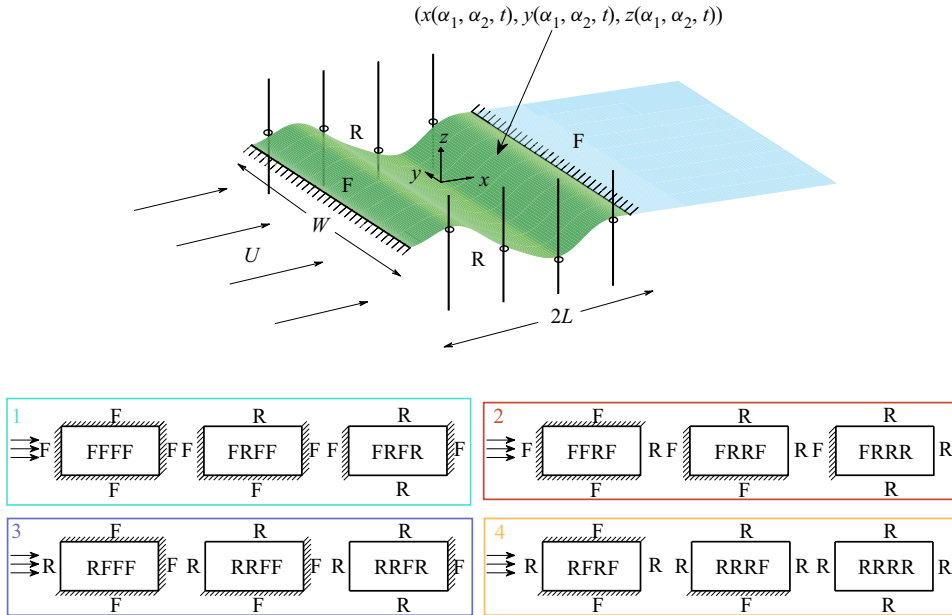
Figure 1. Schematic diagram (in perspective view) showing a 3-D membrane (dark green surface) with fixed leading and trailing edges and free side edges. Along a free edge, points are fixed to massless rings that slide without friction along vertical poles. Here, $U\hat{e}_x$ is the oncoming flow velocity, W is the membrane's spanwise width and $2L$ is the membrane's chord. There is also a flat vortex wake (light blue surface) that emanates from the membrane's trailing edge. In the lower portion of the figure, we also show schematically (in top view) the 12 distinct boundary conditions explored in the current work. The diagonal marks indicate a fixed (F) boundary and other boundaries are free (R). The arrows indicate the far-field flow direction which is the same for each configuration.

and $\alpha_2 \in [-W/2, W/2]$ are the material coordinates, the x and y coordinates of each point in the initially flat state (with a uniform in-plane tension – a 'pretension' – applied by the boundaries).

Each of the four membrane edges is either fixed at zero deflection or free to move in the z direction, perpendicular to the oncoming flow. Then there are $2^4 = 16$ possible boundary conditions, but since the problem is symmetrical with respect to reflection in the x–z plane, we only need to consider 12 distinct boundary conditions, which can be denoted: FFFF, FRFF/FFFR, FRFR, FFRF, FRRF/FFRR, FRRR, RFFF, RRFF/RFFR, RRFR, RFRF, RRRF/RFRR and RRRR (with symmetrical pairs identified). Here, F stands for a fixed edge and R stands for a free edge. The first letter in each label is the leading-edge boundary condition type and the following letters are the boundary conditions moving clockwise around the rectangular membrane looking down from larger z values (bottom of figure 1), as in Gibbs *et al.* (2015). Thus, the second and fourth letters are the side-edge boundary conditions and the third letter is the trailing-edge boundary condition. We will see in the results sections that the dynamics in the 12 cases are naturally classified into four groups, based on whether the leading and trailing edges are fixed or free. Each group is placed in one of the four coloured rectangles in the lower portion of figure 1. We present the results for each group in the four subsections of § 5.2, numbered with the numbers listed at the upper left corner of each group's rectangle in figure 1. We list the equations

for three examples from the set of 12 boundary conditions (and the others are analogous)

$$\text{FRFR:} \quad z(-L, \alpha_2, t) = 0, \; z(L, \alpha_2, t) = 0,$$
$$\partial_{\alpha_2} z(\alpha_1, -W/2, t) = 0, \; \partial_{\alpha_2} z(\alpha_1, W/2, t) = 0, \tag{2.1}$$

$$\text{FRRR:} \quad z(-L, \alpha_2, t) = 0, \; \partial_{\alpha_1} z(L, \alpha_2, t) = 0,$$
$$\partial_{\alpha_2} z(\alpha_1, -W/2, t) = 0, \; \partial_{\alpha_2} z(\alpha_1, W/2, t) = 0, \tag{2.2}$$

$$\text{RRRR:} \quad \partial_{\alpha_1} z(-L, \alpha_2, t) = 0, \; \partial_{\alpha_1} z(L, \alpha_2, t) = 0,$$
$$\partial_{\alpha_2} z(\alpha_1, -W/2, t) = 0, \; \partial_{\alpha_2} z(\alpha_1, W/2, t) = 0. \tag{2.3}$$

Whether the edge is fixed or free affects only the out-of-plane (z-) component of the membrane motion at the edge. In all cases, no in-plane motion of the membrane edges is allowed, i.e. the x- and y-coordinates of the edges are fixed (see figure 1)

$$\text{Upstream/downstream edges:} \; \{x\,(\pm L, \alpha_2, t) = \pm L, \quad y\,(\pm L, \alpha_2, t) = \alpha_2\}, \quad -\frac{W}{2} \leq \alpha_2 \leq \frac{W}{2}, \tag{2.4}$$

$$\text{Side edges:} \; \left\{ x\left(\alpha_1, \pm\frac{W}{2}, t\right) = \alpha_1, \quad y\left(\alpha_1, \pm\frac{W}{2}, t\right) = \pm\frac{W}{2} \right\}, \quad -L \leq \alpha_1 \leq L. \tag{2.5}$$

We start with the stretching energy per unit undeformed area for a thin sheet with isotropic elasticity (described in § 1 of the supplementary material available at https://doi.org/10.1017/jfm.2022.957 and Efrati, Sharon & Kupferman 2009; Alben *et al.* 2019)

$$w_s = \frac{h}{2} \frac{E}{1+\nu} \left(\frac{1}{1-\nu}(\epsilon_{11}^2 + \epsilon_{22}^2) + \frac{2\nu}{1-\nu}\epsilon_{11}\epsilon_{22} + 2\epsilon_{12}^2 \right), \tag{2.6}$$

where E is Young's modulus, ν is Poisson's ratio, h is the membrane's thickness and the strain tensor is

$$\epsilon_{ij}(\alpha_1, \alpha_2, t) = \bar{e}\delta_{ij} + \frac{1}{2}\left(\partial_{\alpha_i}\boldsymbol{r} \cdot \partial_{\alpha_j}\boldsymbol{r} - \delta_{ij}\right). \tag{2.7}$$

Here, $\bar{e}$ denotes a constant prestrain corresponding to the pretension applied at the boundaries and δ_{ij} is the identity tensor, with $i, j \in \{1, 2\}$. We take the variation of the stretching energy

$$W_s = \iint w_s \, d\alpha_1 \, d\alpha_2 \tag{2.8}$$

with respect to the position $\boldsymbol{r}$ to obtain the stretching force per unit material area, i.e. $-\delta w_s/\delta \boldsymbol{r}$.

Integrating by parts to move derivatives off of $\delta \boldsymbol{r}$ terms, we obtain

$$\delta W_s = \frac{Eh}{1+\nu} \oint \left[\left(\frac{1}{1-\nu}\epsilon_{11} \left(\frac{\partial \boldsymbol{r}}{\partial \alpha_1} \cdot \delta \boldsymbol{r} \right) + \frac{\nu}{1-\nu}\epsilon_{22} \left(\frac{\partial \boldsymbol{r}}{\partial \alpha_1} \cdot \delta \boldsymbol{r} \right) + \epsilon_{12} \left(\frac{\partial \boldsymbol{r}}{\partial \alpha_2} \cdot \delta \boldsymbol{r} \right) \right) \upsilon_1 \right.$$
$$+ \left. \left(\frac{1}{1-\nu}\epsilon_{22} \left(\frac{\partial \boldsymbol{r}}{\partial \alpha_2} \cdot \delta \boldsymbol{r} \right) + \frac{\nu}{1-\nu}\epsilon_{11} \left(\frac{\partial \boldsymbol{r}}{\partial \alpha_2} \cdot \delta \boldsymbol{r} \right) + \epsilon_{12} \left(\frac{\partial \boldsymbol{r}}{\partial \alpha_1} \cdot \delta \boldsymbol{r} \right) \right) \upsilon_2 \right] d\sigma$$
$$- \frac{Eh}{1+\nu} \iint \left[\frac{\partial}{\partial \alpha_1} \left(\frac{1}{1-\nu}\epsilon_{11}\frac{\partial \boldsymbol{r}}{\partial \alpha_1} + \frac{\nu}{1-\nu}\epsilon_{22}\frac{\partial \boldsymbol{r}}{\partial \alpha_1} + \epsilon_{12}\frac{\partial \boldsymbol{r}}{\partial \alpha_2} \right) \right.$$
$$+ \left. \frac{\partial}{\partial \alpha_2} \left(\frac{1}{1-\nu}\epsilon_{22}\frac{\partial \boldsymbol{r}}{\partial \alpha_2} + \frac{\nu}{1-\nu}\epsilon_{11}\frac{\partial \boldsymbol{r}}{\partial \alpha_2} + \epsilon_{12}\frac{\partial \boldsymbol{r}}{\partial \alpha_1} \right) \right] \cdot \delta \boldsymbol{r} \, d\alpha_1 \, d\alpha_2. \tag{2.9}$$

953 A32-6

The first integral in (2.9) can be used to obtain the free edge boundary conditions. It is a boundary integral with respect to $d\sigma$, arc length along the boundary in the α_1–α_2 plane; (υ_1, υ_2) is the outward normal in this plane. The integrand in the second integral in (2.9) gives the stretching force per unit material area

$$
f_s = -\frac{\delta w_s}{\delta r} = \frac{Eh}{1+\nu} \left[\frac{\partial}{\partial \alpha_1} \left(\frac{1}{1-\nu} \epsilon_{11} \frac{\partial r}{\partial \alpha_1} + \frac{\nu}{1-\nu} \epsilon_{22} \frac{\partial r}{\partial \alpha_1} + \epsilon_{12} \frac{\partial r}{\partial \alpha_2} \right) \right.
$$
$$
\left. + \frac{\partial}{\partial \alpha_2} \left(\frac{1}{1-\nu} \epsilon_{22} \frac{\partial r}{\partial \alpha_2} + \frac{\nu}{1-\nu} \epsilon_{11} \frac{\partial r}{\partial \alpha_2} + \epsilon_{12} \frac{\partial r}{\partial \alpha_1} \right) \right]. \tag{2.10}
$$

The membrane dynamics is governed by the balance of momentum for a small material element with area $\Delta\alpha_1 \Delta\alpha_2$

$$
\rho_s h \Delta\alpha_1 \Delta\alpha_2 \partial_{tt} r = f_s \Delta\alpha_1 \Delta\alpha_2 - [p](\alpha_1, \alpha_2, t) \hat{n} \sqrt{\det[\partial_{\alpha_i} r \cdot \partial_{\alpha_j} r]} \Delta\alpha_1 \Delta\alpha_2, \tag{2.11}
$$

where ρ_s is the mass per unit volume of the membrane, uniform in the undeformed state; $[p](\alpha_1, \alpha_2, t)$ is the fluid pressure; $\hat{n}$ is the unit normal vector,

$$
\hat{n} = (\partial_{\alpha_1} r \times \partial_{\alpha_2} r) / \| \partial_{\alpha_1} r \times \partial_{\alpha_2} r \|, \tag{2.12}
$$

and $\det[\partial_{\alpha_i} r \cdot \partial_{\alpha_j} r]$ is the determinant of the metric tensor, so $\sqrt{\det[\partial_{\alpha_i} r \cdot \partial_{\alpha_j} r]} \Delta\alpha_1 \Delta\alpha_2$ is the area of the material element in physical space.

We non-dimensionalize the governing equations by the density of the fluid ρ_f, the half-chord L and the imposed fluid flow velocity U. The dimensionless time, space, and pressure jump variables (denoted by tildes) are

$$
\tilde{t} = \frac{t}{L/U}, \quad (\tilde{r}, \tilde{\alpha}_1, \tilde{\alpha}_2) = \frac{(r, \alpha_1, \alpha_2)}{L}, \quad \widetilde{[p]} = \frac{[p]}{\rho_f U^2}. \tag{2.13}
$$

The membrane equation (2.11) becomes

$$
\frac{\rho_s h U^2}{L} \widetilde{\partial_{tt} r} = \frac{Eh}{L(1+\nu)} \left[\widetilde{\partial_{\alpha_1}} \left(\frac{1}{1-\nu} \widetilde{\epsilon_{11}} \widetilde{\partial_{\alpha_1} r} + \frac{\nu}{1-\nu} \widetilde{\epsilon_{22}} \widetilde{\partial_{\alpha_1} r} + \widetilde{\epsilon_{12}} \widetilde{\partial_{\alpha_2} r} \right) \right.
$$
$$
\left. + \widetilde{\partial_{\alpha_2}} \left(\frac{1}{1-\nu} \widetilde{\epsilon_{22}} \widetilde{\partial_{\alpha_2} r} + \frac{\nu}{1-\nu} \widetilde{\epsilon_{11}} \widetilde{\partial_{\alpha_2} r} + \widetilde{\epsilon_{12}} \widetilde{\partial_{\alpha_1} r} \right) \right]
$$
$$
- \rho_f U^2 \widetilde{[p]} \hat{n} \sqrt{\det[\widetilde{\partial_{\alpha_i} r} \cdot \widetilde{\partial_{\alpha_j} r}]}. \tag{2.14}
$$

Dividing (2.14) by $\rho_f U^2$ throughout yields

$$
\frac{\rho_s h}{\rho_f L} \widetilde{\partial_{tt} r} = \frac{Eh}{\rho_f U^2 L(1+\nu)} \left[\widetilde{\partial_{\alpha_1}} \left(\frac{1}{1-\nu} \widetilde{\epsilon_{11}} \widetilde{\partial_{\alpha_1} r} + \frac{\nu}{1-\nu} \widetilde{\epsilon_{22}} \widetilde{\partial_{\alpha_1} r} + \widetilde{\epsilon_{12}} \widetilde{\partial_{\alpha_2} r} \right) \right.
$$
$$
\left. + \widetilde{\partial_{\alpha_2}} \left(\frac{1}{1-\nu} \widetilde{\epsilon_{22}} \widetilde{\partial_{\alpha_2} r} + \frac{\nu}{1-\nu} \widetilde{\epsilon_{11}} \widetilde{\partial_{\alpha_2} r} + \widetilde{\epsilon_{12}} \widetilde{\partial_{\alpha_1} r} \right) \right]
$$
$$
- \widetilde{[p]} \hat{n} \sqrt{\det[\widetilde{\partial_{\alpha_i} r} \cdot \widetilde{\partial_{\alpha_j} r}]}. \tag{2.15}
$$

Thus, the dimensionless membrane equation (dropping tildes) is

$$
R_1 \partial_{tt} r - K_s \left\{ \partial_{\alpha_1} \left(\epsilon_{11} \partial_{\alpha_1} r + \nu \epsilon_{22} \partial_{\alpha_1} r + (1-\nu) \epsilon_{12} \partial_{\alpha_2} r \right) \right.
$$
$$
\left. + \partial_{\alpha_2} \left(\epsilon_{22} \partial_{\alpha_2} r + \nu \epsilon_{11} \partial_{\alpha_2} r + (1-\nu) \epsilon_{12} \partial_{\alpha_1} r \right) \right\}
$$
$$
= -[p] \hat{n} \sqrt{(\partial_{\alpha_1} r \cdot \partial_{\alpha_1} r)(\partial_{\alpha_2} r \cdot \partial_{\alpha_2} r) - (\partial_{\alpha_1} r \cdot \partial_{\alpha_2} r)^2}, \tag{2.16}
$$

where $R_1 = \rho_s h/(\rho_f L)$ is the dimensionless membrane mass density, $K_s = R_3/(1 - \nu^2)$ is a dimensionless stretching stiffness written in terms of $R_3 = Eh/(\rho_f U^2 L)$, the dimensionless stretching rigidity, and we have written out the determinant under the square root explicitly in (2.16). The prestrain $\bar{e}$ in (2.7) is the strain in a membrane under uniform tension $T_0 = K_s \bar{e}$, the 'pretension', one of the main control parameters here, as in our 2-D study (Mavroyiakoumou & Alben 2020). We assume that the thickness ratio h/L is small, but ρ_s/ρ_f may be large, so R_1 may assume any non-negative value. As in Mavroyiakoumou & Alben (2020), we have neglected bending rigidity, denoted as R_2 in Alben & Shelley (2008). In the extensible regime studied here, R_3 is finite, so $R_2 = R_3 h^2/(12L^2) \to 0$ in the limit $h/L \to 0$. For simplicity and for ease of comparison with the 2-D case we set the Poisson ratio ν (the transverse contraction due to axial stretching) to zero. A simple estimate of the maximum tension induced by viscous stresses is provided by the viscous drag on a flat plate, $2.66Re^{-1/2}$ in the present non-dimensionalization (Batchelor 1967), which ranges from $10^{-2.6}$ to $10^{-1.1}$ for Re (the Reynolds number) in the range 10^3–10^6. In this work the pretension ranges from $10^{-1.5}$ to 10^2, but is usually at or above 10^{-1}, so in a large number of cases the viscosity-induced tension is negligible. Therefore, to limit the number of cases under discussion, we neglect the effect of viscosity.

We solve for the flow using the vortex-lattice method, a type of panel method (Katz & Plotkin 2001) that solves for the 3-D inviscid flow past a thin body by posing a vortex sheet on the body to satisfy the no-flow-through or kinematic condition. The vortex sheet is advected into the fluid at the body's trailing edge, thus avoiding a flow singularity there (Katz & Plotkin 2001). The velocity $\boldsymbol{u}$ is a uniform background flow $\hat{\boldsymbol{e}}_x$ plus the flow induced by a distribution of vorticity $\boldsymbol{\omega}$, via the Biot–Savart law (Saffman 1992)

$$\boldsymbol{u}(\boldsymbol{x}) = \hat{\boldsymbol{e}}_x + \frac{1}{4\pi} \iiint_{\mathbb{R}^3} \boldsymbol{\omega}(\boldsymbol{x}', t) \times (\boldsymbol{x} - \boldsymbol{x}')/\|\boldsymbol{x} - \boldsymbol{x}'\|^3 \, d\boldsymbol{x}'. \qquad (2.17)$$

The vorticity is a vortex sheet on the body and wake. With the body surface parametrized by α_1 and α_2, we define a local coordinate basis by $\{\hat{\boldsymbol{s}}_1, \hat{\boldsymbol{s}}_2, \hat{\boldsymbol{n}}\}$

$$\hat{\boldsymbol{s}}_1 = \frac{\partial_{\alpha_1} \boldsymbol{r}}{\|\partial_{\alpha_1} \boldsymbol{r}\|}; \quad \hat{\boldsymbol{s}}_2 = \frac{\partial_{\alpha_2} \boldsymbol{r}}{\|\partial_{\alpha_2} \boldsymbol{r}\|}; \quad \hat{\boldsymbol{n}} \quad \text{from (2.12).} \qquad (2.18)$$

Thus, $\hat{\boldsymbol{s}}_1$ and $\hat{\boldsymbol{s}}_2$ span the body's local tangent plane and $\hat{\boldsymbol{n}}$ is its normal vector. Here, $\hat{\boldsymbol{s}}_1$ and $\hat{\boldsymbol{s}}_2$ are also the tangents to the material lines $\alpha_2 = $ constant and $\alpha_1 = $ constant, respectively. When the body experiences in-plane shear, $\hat{\boldsymbol{s}}_1$ and $\hat{\boldsymbol{s}}_2$ are not orthogonal, but they do not become parallel except for singular deformations that we do not consider.

For the vortex sheet on the body, the vorticity takes the form $\boldsymbol{\omega}(\boldsymbol{x}, t) = \boldsymbol{\gamma}(\alpha_1, \alpha_2, t)\delta(n) = \gamma_1(\alpha_1, \alpha_2, t)\delta(n)\hat{\boldsymbol{s}}_1 + \gamma_2(\alpha_1, \alpha_2, t)\delta(n)\hat{\boldsymbol{s}}_2$, with $\delta(n)$ the Dirac delta distribution and n the signed distance from the vortex sheet along the sheet normal. The vorticity is concentrated at the vortex sheet, $n = 0$, and $\boldsymbol{\gamma}$ is the jump in the tangential flow velocity across the vortex sheet (Saffman 1992). The vorticity can be written similarly in the wake vortex sheet, but a different parametrization is used since α_1 and α_2 are only defined on the body. The nonlinear kinematic equation states that the normal component of the body velocity equals that of the flow velocity at the body (Saffman 1992)

$$\hat{\boldsymbol{n}} \cdot \partial_t \boldsymbol{r} = \hat{\boldsymbol{n}} \cdot \left(\hat{\boldsymbol{e}}_x + \frac{1}{4\pi} \iint_{S_B + S_W} \boldsymbol{\gamma}(\boldsymbol{x}', t) \times (\boldsymbol{r} - \boldsymbol{x}')/\|\boldsymbol{r} - \boldsymbol{x}'\|^3 \, dS_{\boldsymbol{x}'} \right), \qquad (2.19)$$

where S_B and S_W are the body and wake surfaces, respectively. Since $\boldsymbol{r}$ and $\boldsymbol{x}'$ lie on S_B, the integral in (2.19) is singular, defined as a principal value integral.

The pressure jump across the membrane $[p](\alpha_1, \alpha_2, t)$ can be written in terms of the vortex-sheet strength components γ_1 and γ_2 using the unsteady Bernoulli equation written at a fixed material point on the membrane. The formula and its derivation are lengthy so they are given in §2 of the supplementary material, but the form of the pressure jump formula is

$$\partial_{\alpha_1}[p] = G(\boldsymbol{r}, \gamma_1, \gamma_2, \mu_1, \mu_2, \tau_1, \tau_2, \nu_v). \tag{2.20}$$

Here, μ_1 and μ_2 are the tangential components of the average of the flow velocity on the two sides of the membrane, i.e. the dot products of $\hat{\boldsymbol{s}}_1$ and $\hat{\boldsymbol{s}}_2$ with the term in parentheses on the right-hand side of (2.19). Also, τ_1, τ_2 and ν_v are the components of the membrane's velocity in the $\{\hat{\boldsymbol{s}}_1, \hat{\boldsymbol{s}}_2, \hat{\boldsymbol{n}}\}$ basis

$$\tau_1(\alpha_1, \alpha_2, t) = \partial_t \boldsymbol{r} \cdot \hat{\boldsymbol{s}}_1; \quad \tau_2(\alpha_1, \alpha_2, t) = \partial_t \boldsymbol{r} \cdot \hat{\boldsymbol{s}}_2; \quad \nu_v(\alpha_1, \alpha_2, t) = \partial_t \boldsymbol{r} \cdot \hat{\boldsymbol{n}}. \tag{2.21a–c}$$

Equation (2.20) generalizes the 2-D formula from Mavroyiakoumou & Alben (2020, appendix A) to the case of an extensible body in a 3-D flow. We integrate it from the trailing edge using the Kutta condition

$$[p](\alpha_1 = 1, \alpha_2, t) = 0, \tag{2.22}$$

to obtain $[p](\alpha_1, \alpha_2, t)$ at all points on the membrane.

In summary, (2.16), (2.19) and (2.20) are a coupled system of equations for $\boldsymbol{r}$, $\boldsymbol{\gamma}$ and $[p]$ that we can solve with suitable initial and boundary conditions to compute the membrane dynamics.

3. Numerical method

We solve (2.16), (2.19) and (2.20) using an implicit iterative time-stepping approach. At the initial time $t = 0$ the membrane has a very small uniform slope $\partial_{\alpha_1} z / \partial_{\alpha_1} x$ of 10^{-3}, or 10^{-5} if the small-amplitude regime is the focus of interest, and the free vortex wake has length zero. The background flow speed is increased smoothly from 0 to 1 using a saturating exponential function with a time constant 0.2.

We discretize the membrane with a uniform rectangular grid of $M + 1$ and $N + 1$ points in the α_1 and α_2 directions, respectively. The membrane grid becomes deformed in physical space; an example is shown by the black lines on the green membrane surface in figure 2. The vortex sheet is discretized as a lattice of vortex rings, one per membrane grid cell. Each vortex ring consists of four vortex filaments, one along each side of the grid cell. This discretization is a type of vortex-lattice method (Katz & Plotkin 2001; Hiroaki *et al.* 2021). To speed up the computations, we approximate the vortex-sheet geometries as flat, a common approach in vortex-lattice methods (Katz & Plotkin 2001; Hiroaki *et al.* 2021). This occurs in the kinematic equation (2.19), which we solve for $\boldsymbol{\gamma}$ on the body assuming the body position and velocity (i.e. $\boldsymbol{r}$, $\partial_t \boldsymbol{r}$ and $\hat{\boldsymbol{n}}$) and $\boldsymbol{\gamma}$ on the wake are known. The values of $\boldsymbol{r}$, $\partial_t \boldsymbol{r}$ and $\hat{\boldsymbol{n}}$ in (2.19) are those of the true membrane except in the vortex-sheet integrals, where they and $\boldsymbol{x}'$ correspond to the body in its flat position with uniform pretension in the $z = 0$ plane and points in the wake are those of the body's trailing edge, advected at speed 1 in the x-direction. Studies have found that the flat-vortex-sheet approximation is reasonable when bodies undergo small-to-moderate deflections (Izraelevitz, Zhu & Triantafyllou 2017; Fernandez-Escudero *et al.* 2019). The approximation worsens at larger membrane deflections, where the wake deflection would become similarly large and other inviscid approximations (e.g. vortex shedding confined to the trailing edge) would also lose validity. The approximate body and wake vortex sheets lie on the light blue and light
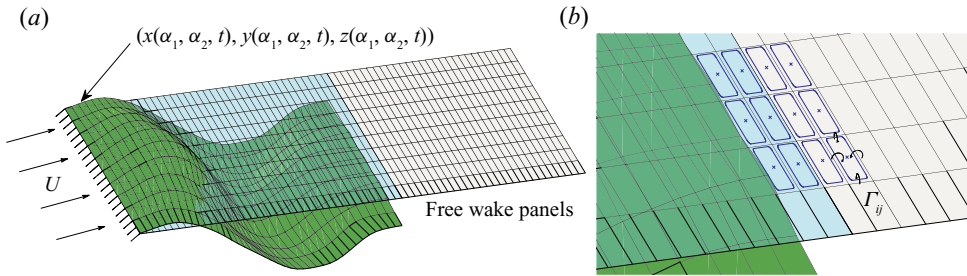
Figure 2. Discretization of the membrane surface into panels with vortex rings. In panel (*a*) we show an example of an FRRR deformed membrane (dark green surface) used for computing the inertial and elasticity terms, together with the flat membrane panels (light blue surface) and flat wake panels (light grey surface) used for the kinematic condition. In panel (*b*) we show a zoomed-in version of the same membrane with a subset of the vortex rings (blue rounded rectangles) on top of the flat membrane and flat-wake panels. The curved arrows illustrate the velocity induced by positive Γ according to the right-hand rule.

grey regions respectively in figure 2. The vortex sheets are approximated by lattices of rectangular vortex rings that lie on the boundaries of the rectangular grid cells. Each line segment in the grid is the support of two vortex lines, one from the vortex ring of each neighbouring grid cell. Figure 2(*b*) shows a schematic example of 12 vortex rings in a 3×4 portion of the lattice that runs across the membrane's trailing edge. The vortex rings are shown as blue rounded rectangles slightly inside each black rectangular boundary, but they actually run along the black edges. The circular arrows show the velocity induced by a single vortex ring marked Γ_{ij}.

The net circulation along each lattice line segment is the difference of the circulations in the two neighbouring vortex rings. The net circulation per unit length in the $\hat{s}_1$ direction converges to γ_1 in the limit of small mesh spacing in that direction, and similarly for γ_2

$$\gamma_1|_{x_{i+1/2},y_j} \approx -\frac{\Gamma|_{x_{i+1/2},y_{j+1/2}} - \Gamma|_{x_{i+1/2},y_{j-1/2}}}{y_{j+1/2} - y_{j-1/2}} \ ; \ \gamma_2|_{x_i,y_{j+1/2}} \approx \frac{\Gamma|_{x_{i+1/2},y_{j+1/2}} - \Gamma|_{x_{i-1/2},y_{j+1/2}}}{x_{i+1/2} - x_{i-1/2}},$$
$$(3.1a,b)$$

using centred difference approximations. We linearly interpolate γ_1 and γ_2 values at the panel edge midpoints from these expressions to values at the panel corners $\{x_i, y_j\}$ and thus obtain $\partial_{\alpha_1}[p]$ in (2.20).

We solve for the strengths of the vortex rings by imposing (2.19) at a set of $\boldsymbol{r}$ (in the integral), called the control points or collocation points in vortex-lattice methods, and here located at the centres of each vortex ring (shown as crosses in figure 2(*b*)). Hess & Smith (1967); Yeh & Plotkin (1986) also placed the control points at the centres of their vortex rings, quadrilaterals and triangles, respectively. Other methods shift the vortex rings and control points downstream by one-quarter mesh spacing, which reproduces certain formulas for the lift and moment on a flat plate (James 1972; Hough 1973; Katz & Plotkin 2001; Moored 2018; Hiroaki *et al.* 2021). Such methods are considered low-order methods, in contrast to higher-order methods that use curved body panel geometries and non-constant polynomial representations for the distribution of circulation or velocity potential on each panel (Willis, Peraire & White 2006; Cole *et al.* 2020). We proceed with the low-order method described here for simplicity and because we find remarkably good agreement with 2-D results using a different discretization method based on Chebyshev polynomials and including the non-flat geometries of the body and wake vortex sheets, including wake roll-up (Mavroyiakoumou & Alben 2020). We also find good agreement

953 A32-10

among results with different mesh sizes, although they indicate spatial convergence below first order (see § 4).

The integral in (2.19) is replaced by a sum that gives the velocity induced by the four sides of all the vortex rings. From Katz & Plotkin (2001), the velocity induced at a point x_p by a straight vortex line segment with circulation Γ that runs from x_1 to x_2 is

$$u = \frac{\Gamma}{4\pi|r_1 \times r_2|^2}\left(\frac{(r_2 - r_1) \cdot r_1}{\|r_1\|} - \frac{(r_2 - r_1) \cdot r_2}{\|r_2\|}\right) \cdot (r_1 \times r_2); \quad r_1 \equiv x_p - x_1, \, r_2 \equiv x_p - x_2. \tag{3.2}$$

When discretized, (2.19) becomes a linear system of equations for the vortex ring strengths. The key advantage of approximating the body and wake vortex sheets as flat is that we can precompute all the matrix entries in the linear system (the 'influence coefficients', i.e. sums of the coefficients of Γ in (3.2)), before the time-stepping iterative solver for the membrane position. For an $M \times N$ lattice of vortex rings on the body and an $M_w \times N$ lattice in the wake (typically $M_w \gg M$), the cost of computing the influence coefficients would be $O(MM_wN^2)$ per iteration within each time step for general membrane and wake shapes, but for flat vortex sheets this can be reduced to a one-time cost of $O(MM_wN)$ (actually less) using repetition in relative positions of control points and vortex rings in the flat wake to change from N^2 to N. We also avoid an even larger cost to evolve the vortex wake position, $O(M_w^2N^2)$, although this could be reduced using fast summation methods (Lindsay & Krasny 2001). The right-hand side vector for the linear system consists of the remaining terms in (2.19), the body velocity and the background flow, using the actual (non-flat) membrane position, and interpolated to give values at the control points.

The algorithm alternates between computing the membrane position at the current time step and updating the vortex wake circulation for the next time step. To compute the membrane position at the current time step, the distribution of circulation in the vortex wake is assumed to be known from the previous steps of the algorithm, and is zero initially. We then use a quasi-Newton iterative method (Broyden's method (Ralston & Rabinowitz 2001)) to solve for the x, y and z components of the membrane position on the interior points of the α_1–α_2 grid, resulting in $3(M-1)(N-1)$ unknowns for the iterative solver.

Broyden's method solves a nonlinear system of equations $f(x) = 0$. In our case x is a vector whose entries are the x, y and z components of the membrane position r on the interior points of the α_1–α_2 grid. Here, f is a vector given by the three components of the membrane equation (2.16), discretized at the interior α_1–α_2 grid points using second-order finite differences for the temporal and spatial derivatives of the membrane position. One-sided spatial differentiation formulas are used near boundaries and backward temporal differentiation formulas are used, with the given initial values for the membrane position and background flow, and zero initial bound circulation (see § 3 of the supplementary material for details). Also, f requires the membrane position boundary values, which are either prescribed (for a fixed boundary) or deduced from the guesses for the values at the interior mesh points (for a free boundary). At each time step Broyden's method produces a sequence of iterates that converges to the solution for x starting from an initial guess, which we choose to be the membrane position at the previous time step. Usually convergence is obtained in just a few iterations.

Given the free wake position and circulation and the guess for r, we compute $\partial_t r$ and $\hat{n}$ and then compute the membrane circulation values by solving the linear system with influence coefficients corresponding to the discretized kinematic equation (2.19). The membrane circulation (and other quantities derived from it and r) are used to compute $\partial_{\alpha_1}[p]$ in the membrane equation (2.16). The pressure jump $[p]$ is then computed by integrating $\partial_{\alpha_1}[p]$ (2.20) with respect to α_1 using the trapezoidal rule and imposing $[p] = 0$

at the trailing edge. All quantities on the right-hand side of (2.20) can be evaluated using the guess for $\boldsymbol{r}$ and the circulations of the vortex rings on the membrane. Some quantities (e.g. γ_1 and γ_2) are computed on the panel edge midpoints and others (e.g. μ_1 and μ_2) on the panel centres; these are extrapolated to the corner points of each panel, where $\partial_{\alpha_1}[p]$ is evaluated. Before integrating $\partial_{\alpha_1}[p]$, we decouple it into two parts, as explained at the end of § 2 of the supplementary material. We integrate one part analytically and the other part numerically using the trapezoidal rule, and apply $[p] = 0$ at the trailing edge. We use this decoupled approach because it gives much better agreement with our previous 2-D computations.

When Broyden's method converges, we obtain the membrane position at the current time step and the circulation values on the membrane. The next step is to update the wake circulation values for the next time step. This is done by moving the vortex rings in the wake and the last row of the vortex rings on the body downstream at speed 1. This is a flat-wake approximation of the more general statement that lines in the wake vortex sheet move at the average of the tangential components of the flow velocity on the two sides of the wake vortex sheet (Saffman 1992). This turns out to be equivalent to the condition that the pressure jump is zero across the wake, and advecting the last row of vortex rings on the membrane into the wake at the trailing-edge flow velocity imposes $[p] = 0$ at the trailing edge, known as the unsteady Kutta condition, which makes flow velocity finite at the trailing edge (Saffman 1992; Katz & Plotkin 2001). The time step is set equal to the streamwise grid spacing, so to move downstream at speed 1 each vortex ring in the wake and along the membrane trailing edge in figure 2 simply shift to the next panel downstream.

In the next section we study the convergence of this numerical method as the membrane grid is refined, and compare the large-span 3-D solutions with 2-D membrane solutions computed using the method in Mavroyiakoumou & Alben (2020).

4. Validation of the 3-D model and algorithm

We now study the effect of spatial grid refinement on the membrane dynamics in test cases using a square membrane at four different combinations of boundary conditions and physical parameters. We then compare 3-D results in the quasi-2-D limit (large span, free side edges) with results at same parameters using our previous 2-D algorithm that had several differences: a Chebyshev–Lobatto mesh and Chebyshev differentiation matrices were used; the kinematic and Kutta conditions were imposed with a Chebyshev–Galerkin method and non-flat vortex sheets; and the full (non-flat) dynamics of the vortex-sheet wake was computed (Mavroyiakoumou & Alben 2020). Three cases are compared: (i) fixed–fixed (2-D) and FRFR (3-D), (ii) fixed–free (2-D) and FRRR (3-D), (iii) free–free (2-D) and RRRR (3-D).

4.1. *Spatial convergence for a square membrane*

Ours and most other implementations of the vortex-lattice method are considered low-order methods, as flat rather than curved body panel geometries are used, as well as vortex rings rather than non-constant polynomial distributions of circulation on each panel (Willis *et al.* 2006; Murua *et al.* 2012; Cole *et al.* 2020). First-order spatial accuracy was found for certain quantities by Margason *et al.* (1985) and Grozdanov (2017) using similar versions of the vortex-lattice method. We study the spatial convergence of our method in four test cases with the following boundary conditions and (R_1, T_0, R_3) values, one from each of the coloured boxes in figure 1: an FFFF membrane with $(R_1, T_0, R_3) = (10^{-0.5}, 10^{-0.5}, 10^0)$, an FFRF membrane with $(10^{0.5}, 10^{-0.75}, 10^1)$, an RFFF membrane

953 A32-12

dx	FFFF, $t_p = 30$ ($10^{-0.5}$, $10^{-0.5}$, 10^0)			FFRF, $t_p = 22$ ($10^{0.5}$, $10^{-0.75}$, 10^1)		
	max $|z|$	Δ max $|z|$	Order	max $|z|$	Δ max $|z|$	Order
2/40	0.5596	0.0171	1.89	0.2169	7.71×10^{-3}	1.55
2/80	0.5425	4.60×10^{-3}	1.46	0.2092	2.64×10^{-3}	0.63
2/160	0.5379	1.67×10^{-3}	. . .	0.2066	1.71×10^{-3}	. . .
2/320	0.5363	. . .	. . .	0.2048	. . .	. . .
dx	RFFF, $t_p = 22$ ($10^{0.5}$, $10^{-0.5}$, 10^1)			RFRF, $t_p = 20$ (10^0, $10^{-0.75}$, 10^1)		
	max $|z|$	Δ max $|z|$	Order	max $|z|$	Δ max $|z|$	Order
2/40	0.2417	4.72×10^{-3}	—	0.2891	9.85×10^{-3}	0.57
2/80	0.2369	—	—	0.2989	6.64×10^{-3}	0.38
2/160	—	—	. . .	0.3056	5.09×10^{-3}	. . .
2/320	—	. . .	. . .	0.3107	. . .	. . .

Table 1. The dx-convergence with fixed d$y = 2/10$ for four cases with boundary conditions and t_p listed at the top, and (R_1, T_0, R_3) below, for membranes with aspect ratio 1. Recall that R_1 is the dimensionless membrane mass, T_0 is the dimensionless pretension and R_3 is the dimensionless stretching rigidity. The change in max $|z|$ between successive dx values and the estimated order of convergence are defined in (4.1a,b).

with ($10^{0.5}$, $10^{-0.5}$, 10^1) and an RFRF membrane with (10^0, $10^{-0.75}$, 10^1). All membranes have aspect ratio one ($W/2L = 1$). We compute the dynamics of the membrane up to a time $t_p \in [20, 30]$ at which large-amplitude oscillatory motion occurs, and record the maximum of $|z(\alpha_1, \alpha_2, t)|$ over the membrane surface and time.

In table 1 we present the maximum $|z|$ values for four different streamwise mesh spacings dx together with the change in max $|z|$ between two successive dx values, and the estimated order of convergence using three successive dx values

$$\Delta \max |z| \equiv \left| \max |z|_{dx} - \max |z|_{dx/2} \right|, \quad \text{Order} \equiv \log_2 \frac{\left| \max |z|_{dx} - \max |z|_{dx/2} \right|}{\left| \max |z|_{dx/2} - \max |z|_{dx/4} \right|}.$$
$$(4.1a,b)$$

We fix the spanwise mesh spacing d$y = 2/10$ (so ten panels cover the span), and recall that d$t =$ dx in all cases, so the time step and streamwise mesh spacing are refined together.

In general, RFFF membranes take a long time to reach the large-amplitude regime (across R_1), so the computations with d$x = 2/160$ and 2/320 were omitted because they were very expensive to compute (due to the large wake size needed). Although the order of convergence is below one in many cases, the Δ max $|z|$ values are quite small. We guess that Δ max $|z|$ is a reasonable estimate of the error in each case, the difference between the computed solution and the solution in the limit d$x \to 0$. As a compromise between computational effort and accuracy, we use d$x = 2/40$ ($M = 40$) in most cases (i.e. throughout § 5), but we present a few comparisons between d$x = 2/40$, 2/80 and 2/160 in the next subsection and find that the results are qualitatively similar.

Table 2 shows the max $|z|$ values at four choices of the spanwise mesh spacing dy, with dx fixed at 2/40 and the other parameters the same as in table 1. The dy convergence is much faster than the dx convergence, presumably because dx sets the resolution near the membrane trailing edge, a particularly sensitive region due to the vortex shedding there (Alben 2009, 2010; Hiroaki *et al.* 2021). The value of Δ max $|z|$ is uniformly small in table 2, at most 4.4 % of the last max $|z|$ value (with d$y = 2/80$). For computational

	FFFF, $t_p = 30$ $(10^{-0.5}, 10^{-0.5}, 10^0)$			FFRF, $t_p = 22$ $(10^{0.5}, 10^{-0.75}, 10^1)$		
dy	max $|z|$	Δ max $|z|$	Order	max $|z|$	Δ max $|z|$	Order
2/10	0.5596	0.0119	2.05	0.2169	7.56×10^{-3}	2.29
2/20	0.5715	2.87×10^{-3}	6.13	0.2093	1.54×10^{-3}	8.62
2/40	0.5744	4.11×10^{-5}	...	0.2078	3.93×10^{-6}	...
2/80	0.5744	...	...	0.2078	...	...
	RFFF, $t_p = 22$ $(10^{0.5}, 10^{-0.5}, 10^1)$			RFRF, $t_p = 20$ $(10^0, 10^{-0.75}, 10^1)$		
dy	max $|z|$	Δ max $|z|$	Order	max $|z|$	Δ max $|z|$	Order
2/10	0.2417	2.14×10^{-3}	0.08	0.2891	7.59×10^{-3}	1.70
2/20	0.2438	2.02×10^{-3}	5.54	0.2815	2.34×10^{-3}	1.63
2/40	0.2418	4.35×10^{-5}	...	0.2792	7.58×10^{-4}	...
2/80	0.2418	...	...	0.2784	...	...

Table 2. The dy-convergence with fixed $dx = 2/40$ for a membrane with aspect ratio 1. The error and order of convergence shown are computed using (4.1*a,b*) but varying dy instead of dx. The (R_1, T_0, R_3) values are the same as in table 1.

efficiency with reasonable accuracy we use $dy = 2/10$ ($N = 10$) in most cases (i.e. throughout § 5). Other recent vortex lattice works have also found that a modest number of grid points in the spanwise direction is sufficient for good accuracy (e.g. Katz & Plotkin 2001, p. 429; Long & Fritz 2004; Nguyen *et al.* 2016, figure 6).

4.2. *Comparisons of 2-D and 3-D results with different mesh sizes*

We now compare 3-D results with free side edges with results from our 2-D algorithm (Mavroyiakoumou & Alben 2020) in cases with both small- and large-amplitude dynamics. We begin by comparing the 2-D fixed–fixed case with the 3-D FRFR case (fixed leading and trailing edges, free side edges). We simulate both cases by starting with a flat membrane at $t = 0$, and for $t > 0$ we keep the leading edge fixed at $z = 0$ and move the trailing edge slightly away from and back to $z = 0$

$$z_{\text{2-D}}(1, t) = z_{\text{3-D}}(1, \alpha_2, t) = 2 \sin \left(\sigma \left(\frac{t}{\eta} \right)^3 e^{-(t/\eta)^3} \right), \quad -\frac{W}{2L} \leq \alpha_2 \leq \frac{W}{2L}, \quad (4.2)$$

where σ is a small constant, 10^{-6}–10^{-3}, and $\eta = 0.2$.

Figure 3(*a,c,e*) plots the z-deflection of the membrane centre (in three dimensions) or midpoint (in two dimensions) vs time at three choices of (R_1, T_0, R_3) (listed in the caption). The 2-D membrane has a Chebyshev–Lobatto mesh with 41 points. In three dimensions, the number of panels in the streamwise direction (M) is 40, 80 or 160, with the aspect ratio $W/2L = 4$, and the number of panels in the spanwise direction (N) 10 in each case. The perturbation size, σ in (4.2), is 10^{-6}. In panels (*a–f*), the 3-D graphs become closer to the 2-D graph as M increases.

To the right of each set of time plots, membrane snapshots are shown, equally spaced in time, for two dimensions (green lines) and three dimensions (with the same colours as in the time plots, for each M), where the line shows the midspan profile. In all three examples, the membranes tend to a steady single-hump shape at large times, as shown for the 2-D
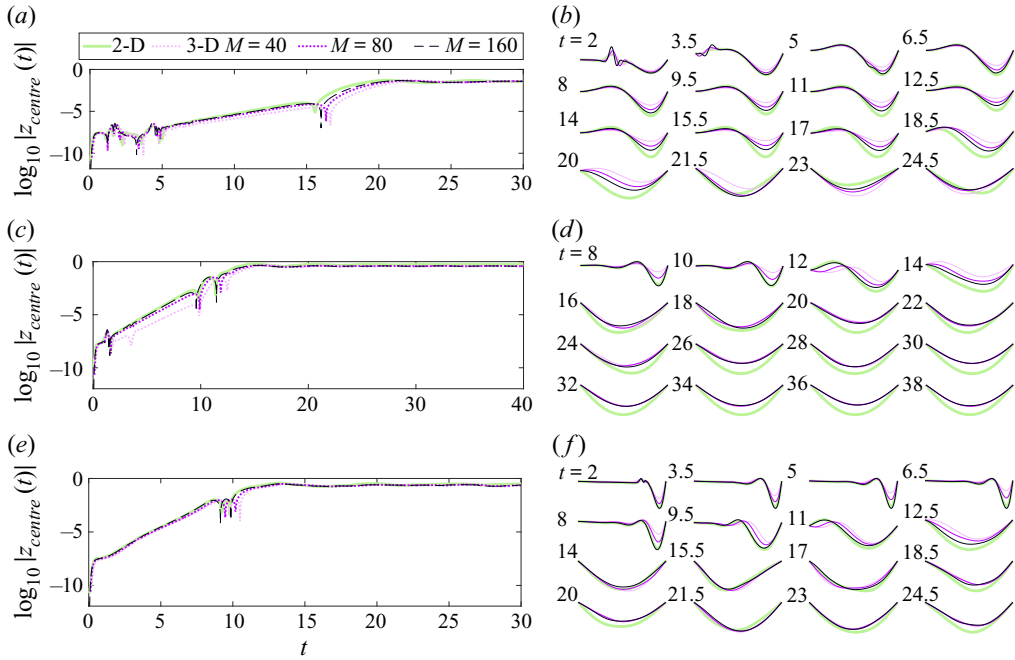
953 A32-14

Figure 3. Comparisons of fixed–fixed (2-D) and FRFR (3-D) computations at three choices of (R_1, T_0, R_3): (a,b) $(10^0, 10^{-0.25}, 10^3)$, (c,d) $(10^{-0.5}, 10^{-0.5}, 10^1)$ and (e,f) $(10^{0.25}, 10^{-0.75}, 10^{1.5})$. Recall that R_1 is the dimensionless membrane mass, T_0 is the dimensionless pretension and R_3 is the dimensionless stretching rigidity. Panels (a,c,e) show plots of $\log_{10} |z_{centre}|$ vs time. Panels (b,d,f) show snapshots of membranes at equally spaced times (labelled at top left). The plots and snapshots are green for 2-D membranes and light pink ($M = 40$), dark pink ($M = 80$) or black ($M = 160$) for 3-D membranes. Here, the aspect ratio $W/2L = 4$, $N = 10$ and $\sigma = 10^{-6}$ in (4.2).

case in Mavroyiakoumou & Alben (2020). In figure 3 there is good qualitative agreement in all the membranes' motions, and good quantitative agreement in most cases, particularly between $M = 160$ (black lines) and two dimensions (green lines) in the small-amplitude (growth) regime. At later times, the 3-D snapshots tend to converge, while the 2-D snapshot is noticeably displaced from them, particularly in panel (d). The 3-D results apparently converge to slightly different states than the 2-D results. Some difference is inevitable due to the finite span in three dimensions and the corresponding difference in the flow and membrane dynamics.

Next we compare the 2-D fixed–free case with the 3-D FRRR case. Now the trailing edge is free, and a small transient perturbation is applied at the leading edge

$$z_{\text{2-D}}(-1, t) = z_{\text{3-D}}(-1, \alpha_2, t) = \sin\left(\sigma \left(\frac{t}{\eta}\right)^3 e^{-(t/\eta)^3}\right), \quad -\frac{W}{2L} \le \alpha_2 \le \frac{W}{2L}. \quad (4.3)$$

Figure 4 compares the membranes' centre-point deflections and snapshots similarly to figure 3 but at three different choices of (R_1, T_0, R_3), given in the figure 4 caption. In the fixed–free case, oscillatory motions occur at large amplitude (Mavroyiakoumou & Alben 2020), and they tend to be periodic rather than chaotic at the $O(1)$ values of R_1 used in figure 4. Again, there is good qualitative agreement in all cases, and good quantitative agreement particularly in the linear growth regime. At large times in panels (a,b) and (e,f) the three 3-D cases are clustered together and are somewhat separate from the 2-D case.
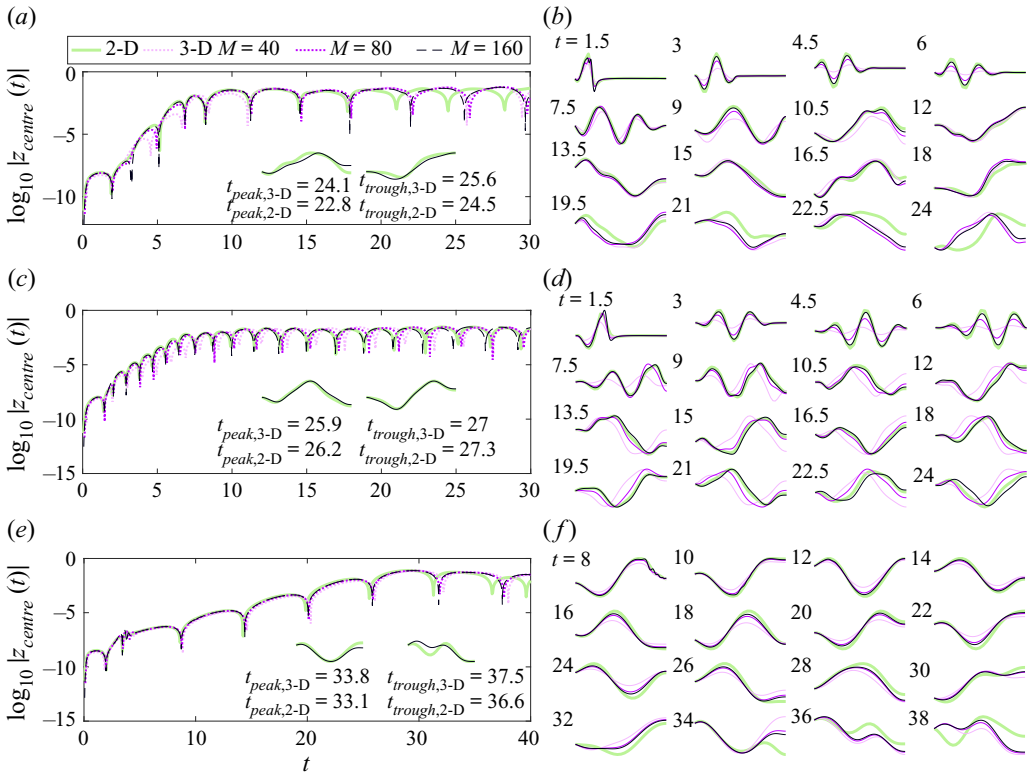
Figure 4. Comparisons of fixed–free (2-D) and FRRR (3-D) computations at three choices of (R_1, T_0, R_3): (a,b) $(10^0, 10^{-1}, 10^2)$, (c,d) $(10^{-0.5}, 10^{-1}, 10^2)$ and (e,f) $(10^{0.5}, 10^{-0.5}, 10^2)$. Panels (a,c,e) show plots of $\log_{10}|z_{centre}|$ vs time. Panels (b,d,f) show snapshots of membranes at equally spaced times (labelled at top left). The plots and snapshots are green for 2-D membranes and light pink ($M = 40$), dark pink ($M = 80$) or black ($M = 160$) for 3-D membranes. Here, the aspect ratio $W/2L = 4$, $N = 10$ and $\sigma = 10^{-6}$ in (4.3).

In panels (c,d) the $M = 160$ and 2-D case are relatively close, even at large times. Within each panel the graphs have somewhat different periods of oscillation at large amplitude, including some abrupt changes in the period, e.g. the 2-D graph near the final time in panels (e,f). However, if we compare the snapshots at qualitatively similar times, i.e. at nearby peaks and troughs of the $\log_{10}|z_{centre}(t)|$ plots, instead of at the same times, then we find better agreement. Comparisons of the 2-D case and the 3-D case with $M = 160$ at nearby peaks and troughs are shown below the time plots, and show better agreement than in the late-time comparisons on the right-hand side of the figure.

Finally, we compare the free–free 2-D case with 3-D RRRR cases. Now the membrane starts with a small non-zero slope

$$z_{2\text{-D}}(\alpha_1, 0) = z_{3\text{-D}}(\alpha_1, \alpha_2, 0) = \sigma\alpha_1, \quad -\frac{W}{2L} \le \alpha_2 \le \frac{W}{2L}, \tag{4.4}$$

for $\sigma = 10^{-3}$. In figure 5 we again compare the membranes' deflections and snapshots for three different (R_1, T_0, R_3) combinations (in the figure caption) with $R_1 = O(1)$ that have qualitatively different dynamics. With all edges free, the membrane can move uniformly upward or downward yet keep the same shape, so there is a translational z motion to consider along with the evolution of the membrane shape. Therefore, on the left-hand side
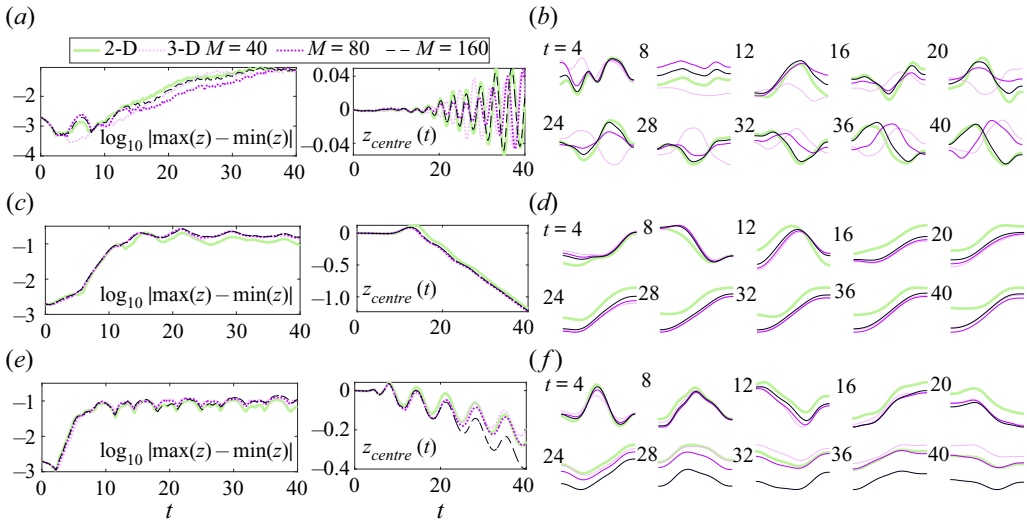
953 A32-16

Figure 5. Comparisons of free–free (2-D) and RRRR (3-D) computations at three choices of (R_1, T_0, R_3): (a,b) $(10^{-0.5}, 10^{-0.75}, 10^1)$, (c,d) $(10^{0.5}, 10^{-0.5}, 10^2)$ and (e,f) $(10^{-0.25}, 10^{-0.8}, 10^2)$. Panels (a,c,e) show plots of $\log_{10} |\max(z) - \min(z)|$ and z_{centre} vs time. Panels (b,d,f) show snapshots of membranes at equally spaced times (labelled at top left). The plots and snapshots are green for 2-D membranes and light pink ($M = 40$), dark pink ($M = 80$) or black ($M = 160$) for 3-D membranes. Here the aspect ratio $W/2L = 4$, $N = 10$ and $\sigma = 10^{-3}$ in (4.4).

we plot the membrane deflection vs time, defined here as $|\max(z) - \min(z)|$, with max and min taken over α_1 (and α_2 for three dimensions), and we also plot $z_{centre}(t)$, which shows the net translational motion. Panel (a) shows an oscillatory motion of z_{centre}, (c) shows a steady translation and (e) shows a combination of the two. As in the fixed–fixed and fixed–free cases, in each panel the agreement in the deflection $|\max(z) - \min(z)|$ is generally best at early times, and at later times there is a more noticeable difference, particularly between the 2-D and 3-D plots in panels (c,d) and (e,f). The snapshots at the right show that in many cases the shapes agree well but there is a translational shift, particularly at $t = 8$ in (b) (where the shift is small, $\approx 10^{-3}$) and at larger times in (f). As in the fixed–free case, there are noticeable phase shifts among the motions at later times for the oscillatory case in panel (b).

In summary, the comparisons of 3-D motions at $M = 40$, 80 and 160 and the 2-D motion have shown good qualitative agreement in the types of dynamics – steady or oscillatory, with or without translation – and good quantitative agreement as well in the magnitudes of the deflections, the frequencies of oscillations and many detailed aspects of the dynamics.

Inviscid simulations of airfoils and flapping plates in two dimensions and three dimensions have shown that the largest computational errors tend to occur in flow quantities near the trailing edge (Katz & Plotkin 2001; Alben 2008*a*, 2010; Hiroaki *et al.* 2021). The Kutta condition makes the flow velocity and pressure jump finite there, but their spatial derivatives across the edge are infinite there in general (Alben 2010), and the numerical solution is sensitive to the mesh near the trailing edge (Alben 2010; Hiroaki *et al.* 2021). For the present simulations, this sensitivity can be seen in the pressure jump distribution near the trailing edge. In figure 6 we plot the pressure jump vs streamwise location along the membrane midspan, $y = 0$, for two different examples of FRRR membranes in the large-amplitude regime, at R_1, T_0 and R_3 given in the figure
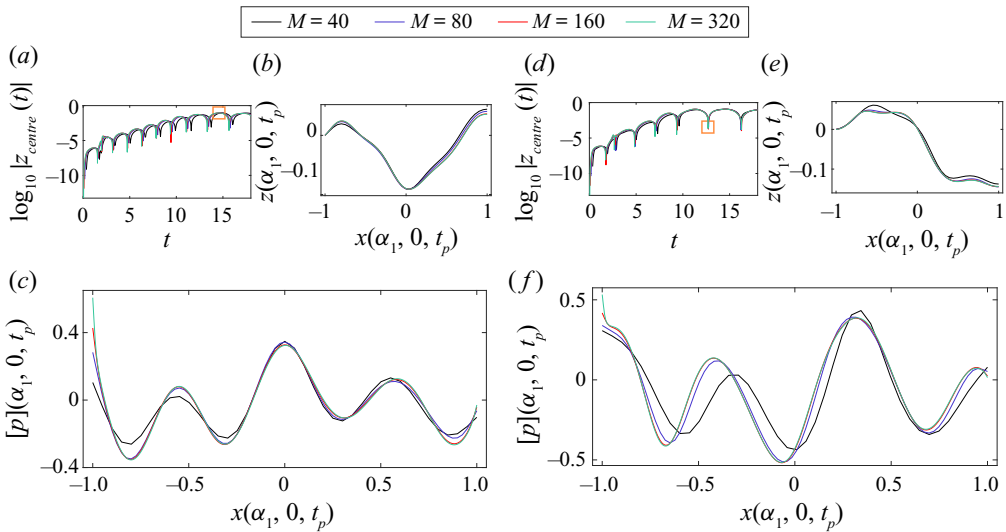
Figure 6. Two examples of how the pressure distribution changes with increasing numbers of streamwise panels. Panels (*a–c*) show plots of $\log_{10}|z_{centre}|$ vs time and $z(\alpha_1, 0, t_p)$ and $[p](\alpha_1, 0, t_p)$ vs $x(\alpha_1, 0, t_p)$, respectively, for an FRRR membrane with $R_1 = 10^{-0.25}$, $T_0 = 10^{-0.75}$ and $R_3 = 10^1$ at times t_p where $|z_{centre}(t)|$ has a peak that is closest to 14.5 (enclosed in the orange square), for each M. Panels (*d–f*) show the same quantities for an FRRR membrane with $R_1 = 10^0$, $T_0 = 10^{-0.75}$ and $R_3 = 10^1$, for the troughs in $|z_{centre}(t)|$ nearest to $t_p \approx 12.6$. The plots are black for $M = 40$, blue for $M = 80$, red for $M = 160$ and green for $M = 320$. Here, the aspect ratio $W/2L = 4$, $N = 10$ and $\sigma = 10^{-4}$ in (4.3).

caption, and for various M listed at the top. Both cases reach oscillatory large-amplitude states, shown by the centre deflection vs time in panels (*a*) and (*d*), respectively. In panels (*b*) and (*e*) we compare the midspan deflections that occur at $|z_{centre}|$ peaks near $t = 14.5$ and troughs near 12.6, respectively – the peaks and troughs that occur in the orange boxes of panels (*a,d*). For each M the times of the peaks/troughs are slightly different due to phase shifts, as in the snapshot comparisons in figure 4(*a,c,e*). Panels (*c,f*) show the midspan pressure jump distributions at these times. The pressure jump distributions are more oscillatory and have larger deviations at these M than the deflections (*b,e*), perhaps because in the membrane equation (2.16) $[p]$ is balanced by terms that include second spatial derivatives of deflection, so z is smoother than $[p]$. We also find oscillations with similar spatial length scales in $\partial_{tt}z$ (not shown), perhaps indicating the effect of membrane inertia and added mass on $[p]$. The pressure jump distributions in (*c,f*) only approximately reach zero at the trailing edge, more closely for larger M, which also resemble the generic square-root behaviour there, as well as the generic inverse-square-root behaviours at the leading edge (Golberg 1990; Alben 2009, 2010). Although the deviations from $M = 40$ to 320 are significant, the overall form of the $[p]$ and z distributions at $M = 40$ are reasonable approximations to those at $M = 320$.

Now we briefly present a comparison of the dynamics in two and three dimensions using different numbers of panels across the span for three dimensions: $N = 10$, 20 and 40. Figure 7 shows comparisons of (*a*) fixed–fixed, (*b*) fixed–free and (*c*) free–free 2-D cases with the corresponding 3-D cases at $M = 40$ and aspect ratio 4. The 3-D plots converge more rapidly here with increasing N than with increasing M in the previous figures, similarly to tables 1 and 2. In the remainder of this work we use $N = 10$.
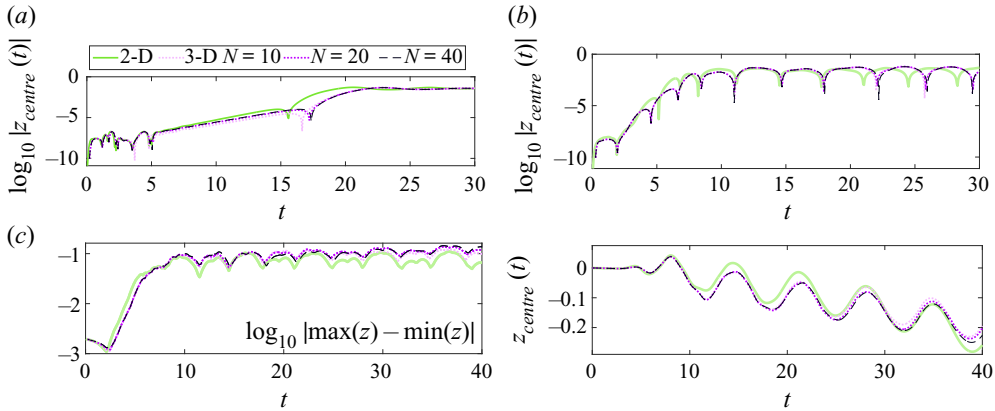
953 A32-18

Figure 7. Comparisons of 2-D and 3-D membrane deflections at three boundary conditions and (R_1, T_0, R_3) values: (*a*) fixed–fixed vs FRFR at $(10^0, 10^{-0.25}, 10^3)$; (*b*) fixed–free vs FRRR at $(10^0, 10^{-1}, 10^2)$; and (*c*) free–free vs RRRR at $(10^{-0.25}, 10^{-0.8}, 10^2)$, where both $\log_{10} |\max(z) - \min(z)|$ and z_{centre} are plotted, at left and right, respectively. The plots are green for 2-D membranes and light pink ($N = 10$), dark pink ($N = 20$) or black ($N = 40$) for 3-D membranes. Here, 41 Chebyshev–Lobatto points are used in two dimensions and for the 3-D cases $W/2L = 4$, $M = 40$ and $\sigma = 10^{-6}$, 10^{-6} and 10^{-3}, respectively in (*a–c*).

We have compared the small- and large-amplitude dynamics in two and three dimensions at several (R_1, T_0, R_3) values, and shown the effect of varying the numbers of streamwise and spanwise panels in three dimensions, M and N, at aspect ratio 4. Next, we compare the dynamics across a much larger set of R_1 and T_0 values, but restricted to the small-amplitude regime (where R_3 has a negligible effect). We also show the effect of increasing the 3-D membrane aspect ratio from 1 to 8, approaching the 2-D limit.

4.3. *Comparison of stability boundaries and mode shapes in two and three dimensions*

The small-amplitude membrane dynamics can be organized in terms of the stability boundary in R_1–T_0 space. We again apply the small perturbations (4.2)–(4.4) to the FRFR, FRRR and RRRR membranes, across a grid of values in R_1–T_0 space. At each R_1 we find exponential decay in membrane deflections above a critical T_0 and exponential growth below this T_0 (followed by large-amplitude, nonlinear dynamics). The stability boundary is the curve of critical T_0 vs R_1, and is found by interpolating between neighbouring T_0 points with positive and negative growth rates.

In figure 8 we compare the stability boundaries in the 2-D fixed–fixed (*a*), fixed–free (*b*) and free–free (*c*) cases with the 3-D FRFR, FRRR and RRRR cases, respectively, with 3-D aspect ratios 1, 2, 4 and 8. Two stability boundaries are shown for the 2-D case. The orange lines, from Mavroyiakoumou & Alben (2020), are calculated from the growth rates in time-stepping simulations starting from small perturbations, as in the 3-D cases here. The red lines, from Mavroyiakoumou & Alben (2021*b*), are calculated by linearizing the 2-D equations and solving the nonlinear eigenvalue problem; the imaginary parts of the eigenvalues are the growth rates. The eigenvalue method was able to identify very small positive growth rates at $R_1 \geq 10^2$, too small to be distinguishable from no growth or very slow decay in the time-stepping method. Here, the red line has a sharply upward slope (similar to Tiomkin & Raveh (2017)), unlike the orange line. The stability boundaries for the 3-D cases with aspect ratios 1, 2, 4 and 8 range from light blue to dark blue. In (*a*) and at large R_1 in (*b,c*) the boundaries tend towards the 2-D boundaries as aspect
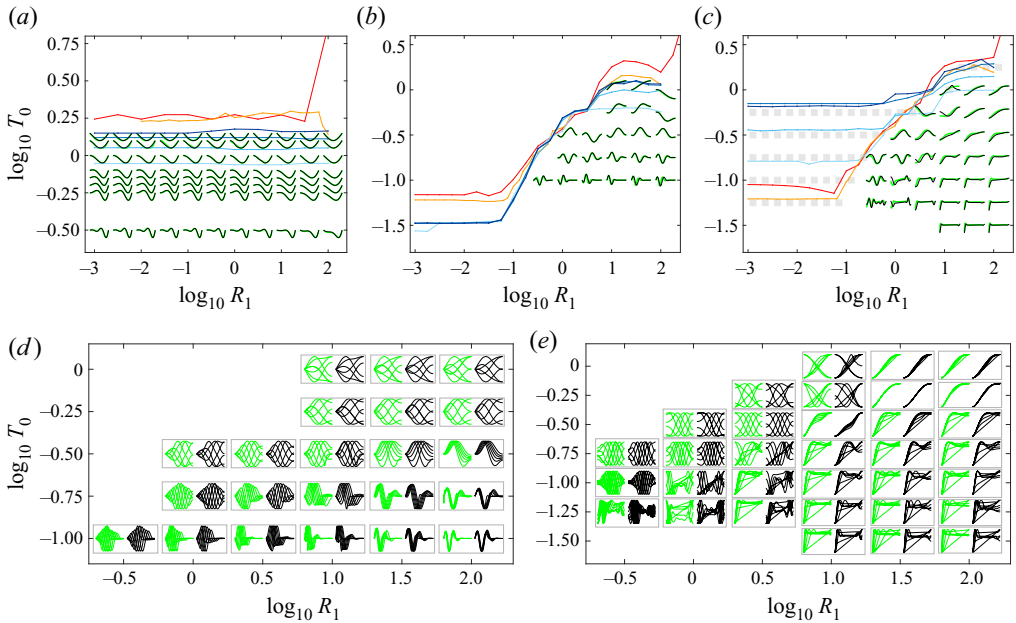
Figure 8. Comparisons of stability boundaries in two dimensions (orange from Mavroyiakoumou & Alben 2020; red from Mavroyiakoumou & Alben 2021b) and three dimensions with aspect ratios 1, 2, 4 and 8 (ranging from light blue to dark blue) for (a) fixed–fixed and FRFR, (b) fixed–free and FRRR and (c) free–free and RRRR cases. Below the stability boundary, 3-D midspan profiles with aspect ratio 8 (black) are compared with 2-D profiles (green) during the linear growth regime. Here, $R_3 = 10^1$, $N = 10$, $M = 40$ (for FRFR and FRRR membranes) and $M = 80$ (for RRRR membranes) for all aspect ratios.

ratio increases. As in studies of 3-D flexible plates (Eloy, Souilliez & Schouveiler 2007; Eloy *et al.* 2008; Banerjee *et al.* 2015), more bodies are unstable at high aspect ratio, i.e. the stability boundary moves up as the aspect ratio increases. In the region of instability for aspect ratio 8, we compare the aspect ratio 8 midspan snapshots at small amplitude (black lines) with the 2-D snapshots (green lines) over a range of R_1 and T_0. In (a), all the membranes lose stability by divergence without flutter, so the membranes' deflections grow exponentially without change of shape. The snapshots show the eigenmode shapes, which become more fore–aft asymmetric as T_0 decreases, although at large amplitude the membranes tend to single-hump shapes that are nearly fore–aft symmetric as in figure 3. The agreement is uniformly very good between two and three dimensions in panel (a).

Panel (b) shows the same comparison for the 2-D fixed–free and 3-D FRRR cases. The modes are somewhat underresolved for $T_0 < 10^{-1}$ and the growth rates in two and three dimensions do not agree well, so we omit the membrane snapshots in this region of the parameter space. Even with a much finer mesh, the fastest growing 2-D modes are difficult to resolve in this region using an eigenvalue solver (Mavroyiakoumou & Alben 2021b). This underresolution may affect the apparent lack of convergence of the 3-D stability boundaries with increasing aspect ratio to the 2-D boundaries at small R_1. At moderate R_1 ($\in [10^{-0.5}, 10^{0.5}]$), interestingly, the stability boundaries approximately coincide at all aspect ratios, while at larger R_1 the stability boundaries shift upward with increasing aspect ratio similarly to panel (a). Unlike in panel (a), here the snapshots oscillate and change shape in the small-amplitude growth regime. In panel (d) we show sets of six snapshots for the 2-D (green) and 3-D (black) cases during time intervals between two consecutive

peaks or troughs in the graph of $z_{centre}(t)$. The snapshots are normalized to have uniform maximum deflections. The agreement between two and three dimensions is very good in all cases. The third snapshots in each sequence are overlaid in the instability region in panel (*b*). In (*b,d*) the values of $\log_{10} R_1$ and $\log_{10} T_0$ for each set of snapshots are the multiples of 0.5 and 0.25 respectively that intercept each set.

Panels (*c,e*) show the same comparison for the 2-D free–free and 3-D RRRR cases. The stability boundaries and resolution issues are similar to those in panel (*b*), but here adequate resolution is obtained down to smaller T_0. At small R_1 values, the 3-D stability boundaries actually move away from the 2-D boundaries as the aspect ratio increases. This is due to special cases with very small but positive growth rates over a large range of T_0 at small R_1. Cases with aspect ratio 8 and growth rates < 0.04 are marked in panel (*c*) by grey boxes. Such cases only occur close to the stability boundary at large R_1, as expected, but occur over a large range of T_0 from the dark blue line to the orange (2-D) line at small R_1. Below the orange line, the 3-D growth rates abruptly become much larger, so setting aside the cases with very slow growth, we have better agreement in the stability boundary for two and three dimensions with aspect ratio 8. There is nothing obviously wrong with these slow-growth cases (such as very jagged shapes or non-physical motions); unlike most of the results in this section, they may be a case where the 3-D large-span dynamics is qualitatively different from the 2-D dynamics.

The agreement between the snapshots in two (green) and three dimensions (black) in panels (*c,e*) is generally very good, although not quite as good as in (*b,d*), particularly in some cases at $T_0 = 10^{-1}$ and $10^{-1.25}$ that are clearly underresolved. In (*c,e*) higher resolution is used: $M = 80$ for RRRR and 81 Chebyshev–Lobatto points are used in two dimensions, vs 40 and 41 respectively in (*a,b,d*). In four cases at the upper right of (*c,e*) $|z_{centre}|$ grows without oscillating, similarly to a divergence instability, so the six snapshots are equally spaced over a large portion of the small-amplitude regime.

We have presented a broad range of evidence of good qualitative agreement between the 2-D and 3-D dynamics, even with fairly modest 3-D mesh sizes ($M = 40$ and $N = 10$ in most cases) and other significant computational differences. In two dimensions we used a Chebyshev–Lobatto mesh, computed wake roll-up and used a Galerkin method for the kinematic equation and Kutta condition, with a non-flat body and wake in the kinematic condition. In three dimensions we used a uniform mesh, flat approximate vortex sheets on the body and wake and a collocation method for the kinematic condition. We now proceed to study and classify the dynamics of 3-D membranes with square aspect ratios at all 12 of the boundary conditions in figure 1.

5. Membrane dynamics across parameter space for 12 boundary conditions

We now broadly classify the membrane dynamics with respect to R_1, T_0 and R_3 at all 12 combinations of fixed and free boundary conditions at the edges. In a few cases the large-amplitude dynamics does not seem to depend very strongly on aspect ratio, so we set it to 1 here, but it would be good to explore this parameter in future work.

To find where the membranes are unstable, we apply the perturbation (4.4) with $\sigma = 10^{-5}$ for all 12 boundary conditions at a large number of R_1 and T_0 values, and as before we find the critical T_0 at each R_1 by interpolation of growth rates.

Figure 9 shows the stability boundaries for the 12 boundary conditions, listed at right. Based on the locations of the boundaries and the qualitative features of membranes' large-amplitude dynamics (presented later), the 12 boundary conditions naturally fall into
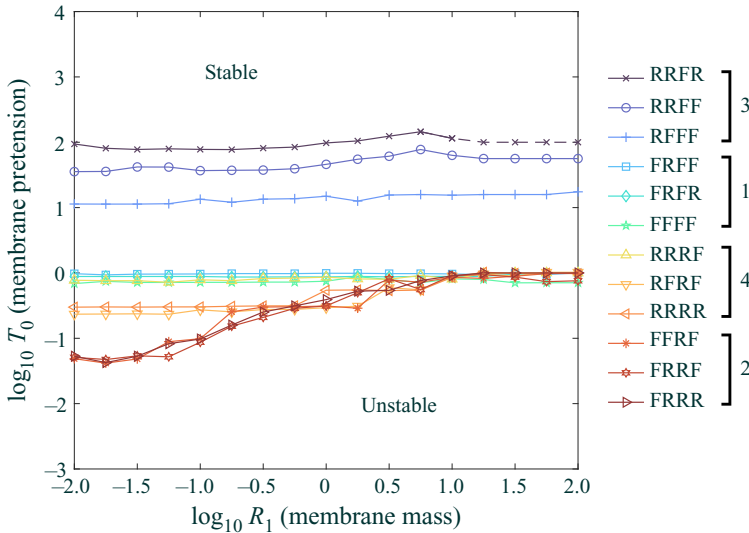
Figure 9. Stability boundaries for the 12 boundary conditions, listed at right, and placed in four groups that depend on only the leading- and trailing-edge conditions, as in figure 1.

four groups, listed at right in figure 9 and shown in figure 1, and determined by only the leading- and trailing-edge conditions. The conditions at these edges seem to determine the qualitative behaviours of the membranes' dynamics more strongly than the side-edge conditions. However, the side edges can still have important effects, particularly for the large-amplitude results we will present.

In the 2-D vs 3-D comparisons, we have already shown one stability boundary from three of the four groups: FRFR from group 1, FRRR from group 2 and RRRR from group 4. The other stability boundaries within these groups are similar – nearly flat in group 1, upward sloping in group 2 and either flat or upward sloping in group 4, although the flatness at small R_1 for RRRR is affected by the slow-growth cases in figure 8(c). Perhaps due to these cases, there is more variability in the boundaries of group 4 at small R_1, while the boundaries are more uniform across groups 1 and 2. The data for group 3, with the leading edge free and trailing edge fixed, are completely new, and stand out from the other groups in two respects. The group 3 stability boundaries are orders of magnitude higher in T_0 than those of the other groups. There is also about an order-of-magnitude variation of the critical T_0 within group 3, higher (less stable) with more side edges free. At large R_1 it is difficult to distinguish slow growth and slow decay, particularly for RRFR, so the stability boundary is dashed to indicate this lack of certainty.

In the supplementary material, figure S1 marks (R_1, T_0) pairs where the small-amplitude instability corresponds to divergence or flutter with divergence, for each of the 12 boundary conditions. Divergence (without flutter) is most common for group 1 (fixed–fixed), while flutter with divergence is more common for the other three groups.

5.1. *Large-amplitude scaling laws*

We now study how key quantities – the typical magnitudes of deflections, and for unsteady cases, frequencies of oscillations – depend on R_1, T_0 and R_3 in the large-amplitude regime. We set the perturbation magnitude σ to 10^{-3} for groups 1, 2 and 4 and 10^{-2}

953 A32-22

for group 3, larger than the 10^{-5} value we used for the stability boundaries, to reach the large-amplitude regime faster. We also tested a few cases with different σ: $\pm 10^{-5}$ and several values ranging from 10^{-3} to 10^{-1}. With $\sigma = -10^{-5}$ we obtained the mirror image of the large-amplitude steady state with $\sigma = 10^{-5}$. With different positive σ and all other parameters the same, in most cases the same large-amplitude steady state was found (static or oscillatory). However, we did find one RFRF case where $\sigma = 10^{-3}$, 10^{-2} and 0.03 gave one steady shape and $\sigma = 0.06$ and 0.1 gave a different steady shape.

In our 2-D work (Mavroyiakoumou & Alben 2020, 2021*b*,*a*) we also studied the typical spatial wavenumbers of membrane deformations, but these are somewhat difficult to quantify precisely without higher spatial resolution, which is more feasible computationally in two dimensions. However, there is sometimes a correlation between wavenumbers and frequencies, which are computed here.

In figure 10 we show how the time-averaged deflection depends on R_3 at several fixed values of R_1 (listed in the legends of panels (*a*,*c*,*d*)) and T_0 for all 12 boundary conditions. We define the time-averaged deflection of the membrane as the maximum membrane deflection minus the minimum deflection, averaged over time

$$\langle z_{defl} \rangle \equiv \frac{1}{t_2} \int_{t_1}^{t_1+t_2} \left(\max_{-1 < \alpha_1, \alpha_2 < 1} z(\alpha_1, \alpha_2, t) - \min_{-1 < \alpha_1, \alpha_2 < 1} z(\alpha_1, \alpha_2, t) \right) \mathrm{d}t, \qquad (5.1)$$

where t_1 and t_2 are sufficiently large that $\langle z_{defl} \rangle$ changes by less than 1 % with further increases in these values. As in the 2-D studies (Mavroyiakoumou & Alben 2020, 2021*a*), deflection scales as $1/\sqrt{R_3}$ at moderate and large R_3 in all 3-D cases. The scaling begins at larger R_3 for the third column, so the R_3 range there is a factor of 10^2 higher than in the other columns. At $R_3 = 10^2$, the deflection magnitudes are generally much higher in column 3 than in the other columns. Selected T_0 values are shown in figure 10 but the same scaling holds at other T_0 values, two of which are shown in the Appendix. We briefly explain the $1/\sqrt{R_3}$ scaling similarly to Mavroyiakoumou & Alben (2020). We expand terms in the z component of the membrane equation (2.16) in the limit of small deflections, by inserting Taylor series for z and its derivatives. T_0 and R_3 enter through the $\bar{e}$ and K_s terms respectively. T_0 multiplies $(\partial_{\alpha_1}^2 + \partial_{\alpha_2}^2)z$ and R_3 multiplies a term that is cubic in derivatives of z. Using the kinematic and pressure jump equations, (2.19) and (2.20), we find that γ_2 is linear in z and therefore so is $[p]$ and the $[p]$ term in (2.16). At steady state, the amplitude is set by a balance of the destabilizing $[p]$ term and the stabilizing R_3 term; the T_0 term is similar in magnitude to these terms near the stability boundary, and becomes insignificant at smaller T_0. Balancing $R_3 O(|z|^3)$ and the $O(|z|)$ pressure term, we have $|z| \sim R_3^{-1/2}$.

In the third column, smaller R_1 values (listed in the top panel) are used compared with the other columns, because the third-column cases did not reach large amplitude within 350 time units at the larger R_1. In a few cases data are omitted because membranes were stable (FFRF with $R_1 = 10^{-0.5}$) or did not attain steady-state motions by $t = 350$ (RRFF and RRFR with $R_1 = 10^{0.5}$).

The other main quantity we measure is the membrane's frequency of oscillation. This is calculated as the reciprocal of the period of oscillation, the time between successive peaks in $z_{centre}(t)$ near the end of the computation (typically $t = 350$). We plot the frequency data in figure 11, similarly to the amplitude data in the previous figure, but now vs R_1, the most important parameter for frequency, at various fixed values of T_0 and R_3 (listed in the titles and in the legends in the first two columns, respectively). Unlike the amplitude, the membranes' shapes and frequencies do not vary much with R_3.
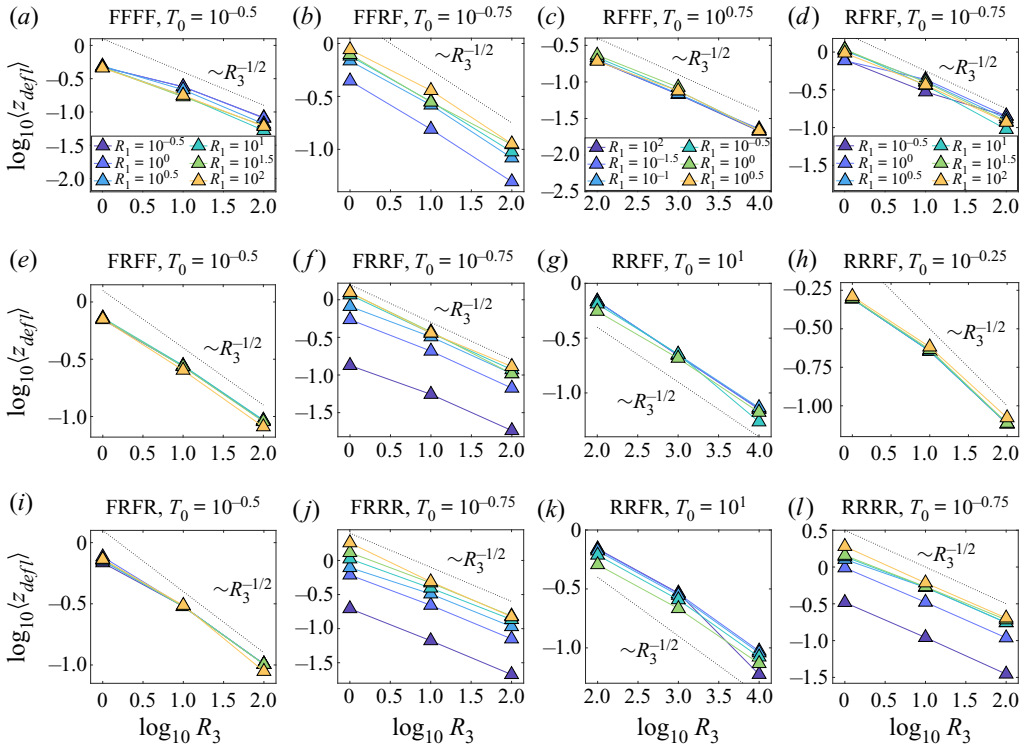
Figure 10. Time-averaged deflections of the membranes (defined by (5.1)) vs R_3 for various R_1 (listed in the top panel of each column, i.e. panels (a,c,d), except (column 2) which uses the same values as panel (a)) and fixed T_0 for all 12 boundary conditions. Recall that R_1 is the dimensionless membrane mass, T_0 is the dimensionless pretension and R_3 is the dimensionless stretching rigidity. Panels (a,e,i), (b,f,j), (c,g,k) and (d,h,l) correspond to groups 1–4 in figures 1 and 9. The dotted black line in each panel indicates the scaling $R_3^{-1/2}$.

In most cases with large R_1 ($\in [10^1, 10^2]$) and some cases with moderate R_1 ($\in [10^0, 10^1]$), the frequency approximately scales as $1/\sqrt{R_1}$, as in the large-amplitude 2-D studies Mavroyiakoumou & Alben (2020, 2021a). The scaling can be explained in two or three dimensions by balancing the $R_1 \partial_{tt} z$ term in the membrane equation with the other terms, which are independent of R_1. Assuming a period of oscillation T, we have $R_1 \partial_{tt} z \sim R_1 z / T^2 \sim O(z)$ for the remaining terms (i.e. the $[p]$ term), so at large R_1 the frequency $= 1/T \sim 1/\sqrt{R_1}$.

There is more variability in the frequency dependence on R_1 than in the amplitude dependence on R_3, for a few main reasons. At large R_1, the oscillation period is longer, so longer times are needed to reach a steady state, and the estimates of period and frequency are based on smaller and perhaps noisier data sets. The oscillations are periodic in some cases but chaotic in others, and in the latter cases the frequency is only a rough estimate of the long-time average. Finally, the oscillatory motion may change qualitatively (e.g. the membrane shapes may change) as R_1 increases in the ranges considered here, which may cause deviations from the simple $1/\sqrt{R_1}$ scaling law.

At small R_1 the frequency typically plateaus here (in the first and third columns). A different behaviour was seen in 2-D simulations of tethered membranes in Mavroyiakoumou & Alben (2021a) which were similar to the 2-D free–free case.
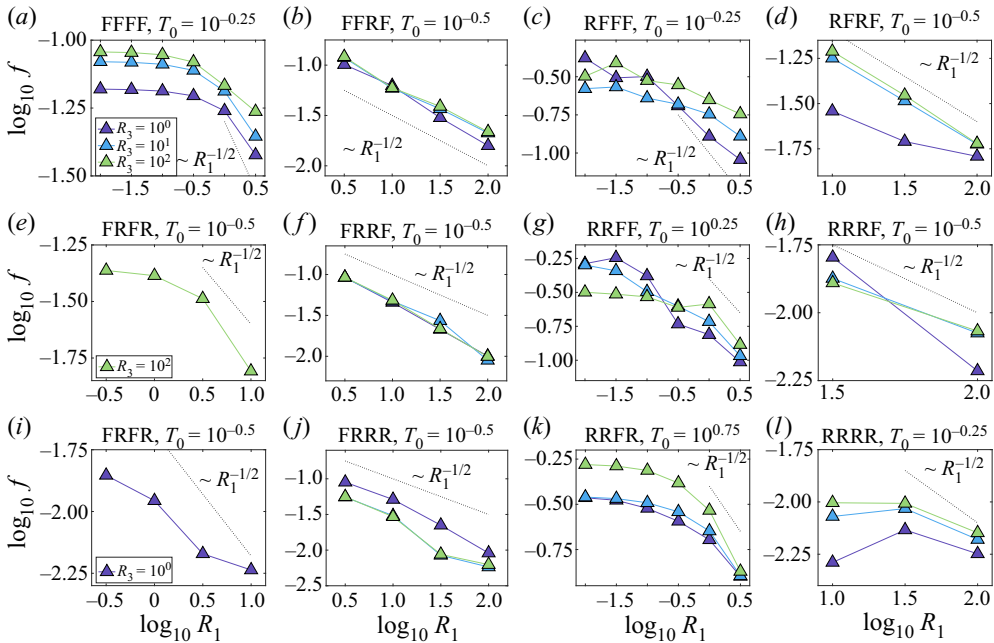
Figure 11. Plots of mean frequency $\log_{10} f$ vs mass density $\log_{10} R_1$ with various R_3 and fixed T_0 values for all 12 boundary conditions. Panels (a,e,i), (b,f,j), (c,g,k), (d,h,l) correspond to groups 1–4 in figures 1 and 9. The dotted black line in each panel indicates the scaling $R_1^{-1/2}$.

There, the frequencies scaled as $R_1^{-5/6}$ at small R_1 and the shapes had very sharp spatial features that required hundreds of points in the streamwise direction to resolve, much higher resolution than we use here in three dimensions. In the corresponding case here, the fourth column of figure 11, we have a limited set of data at small R_1 (at different T_0 than in the fourth column) that show increasing frequencies as R_1 decreases, but it is difficult to characterize the scaling behaviour. At small R_1 one might expect a plateau if the limit $R_1 \to 0$ is a regular perturbation problem, e.g. if the membrane shape does not change much in the limit $R_1 \to 0$, as seems to occur in the first and third columns. However, if the membrane becomes ever wavier as R_1 decreases, the frequency may also diverge, consistent with the 2-D tethered membrane data in Mavroyiakoumou & Alben (2021a) and the closely related problem of a fixed–free flag with bending rigidity (Alben 2022). The fourth and second columns, respectively, are similar to these cases.

The highest frequencies occur in the third column, and these are much higher than in the first column at the same R_1. The third-column frequencies are only moderately higher than those in the second column at the R_1 where both are given, $10^{0.5}$.

One interesting difference with two dimensions that we will discuss further in the next section is that in three dimensions we find many cases of oscillatory membranes with leading and trailing edges fixed, corresponding to the frequencies in the first column. In two dimensions, all physically reasonable fixed–fixed cases assumed steady single-hump shapes. In panel (e) data are only presented at $R_3 = 10^2$ and in panel (i) data are only presented at $R_3 = 10^0$, because the membranes did not oscillate at the other R_3 values across the full range of R_1 shown at these T_0.

5.2. *Large-amplitude dynamics*

We have presented basic scaling relationships for the amplitudes and frequencies of steady-state large-amplitude membrane motions. In this section we characterize the types of motions – e.g. a shape that is steady, or with periodic or chaotic oscillations – across all 12 boundary conditions. We consider in turn each of the four groups in figure 1, determined by the conditions at the leading and trailing edges. We use three values of the stretching rigidity parameter R_3: 10^0, 10^1 and 10^2. Somewhat below 10^0, deflections become unrealistically large in some cases. At $R_3 = 10^2$, the motions generally approximate the large-R_3 asymptotic regime.

We consider values of T_0 that are relatively close to the stability boundary, within 1–1.5 orders of magnitude of it. In general, as T_0 decreases, our algorithm requires more iterations for convergence at a given time step. At T_0 far below the stability boundary ($\gtrsim 1.5$ orders of magnitude), the iterative method in our computational method tends to stagnate without converging at an early time step. In some cases, the stagnation occurs after a sharp angular feature appears in the membrane shape. Presumably larger T_0 inhibits the formation of such features. By contrast, our 2-D algorithm from Mavroyiakoumou & Alben (2020, 2021*a*) was able to compute at arbitrarily small T_0, where the T_0 term became insignificant compared with the R_3 term in the total stretching force. There we found only modest changes in the dynamics as T_0 increased from zero to the stability boundary, so possibly the 3-D results here indicate what would happen at very small T_0, but we defer this question to future work.

In each case we consider a wide range of membrane mass R_1, from small to large. Incidentally, we find that the iteration count increases at smaller R_1, but this does not prevent convergence, unlike at small T_0.

5.2.1. *Leading and trailing edges fixed (FFFF, FRFF, FRFR)*
We begin with membranes whose leading and trailing edges are fixed at zero deflection (group 1 in figures 1 and 9). Figure 12 shows typical motions and where they occur in parameter space. Each row of the top 3×3 array of panels corresponds to different side-edge conditions (FFFF, FRFF or FRFR), and each column to a different R_3 value (10^0, 10^1 or 10^2). The different colours in each panel indicate where different types of motions occur in R_1–T_0 space, with representative examples below. Purple is used for steady single-hump shapes, green for small oscillations (periodic or not) about single-hump shapes, and yellow for up–down symmetric oscillations, usually periodic. Small black dots indicate periodic cases. Blue is used for cases that had slowly decaying oscillations at $t = 350$, and could approach the green or purple states at later times. Such cases occur at large R_1 and the oscillations tend to be less periodic than at smaller R_1. A few white regions in the upper corners of the FFFF panels indicate motions that were still in the exponential growth regime at $t = 350$, while cases in the white region in the FRFR panel at $R_3 = 10^0$ failed to converge at an early time. The three rows at the bottom of figure 12 show representative examples of the membrane motions in the purple, green and yellow regions. Just to the right of small rectangles with these colours, the motions are shown by sequences of 11 midspan snapshots (overlaid), and then further to the right, smaller sequences of four 3-D snapshots, arrayed horizontally. All these sequences are for FFFF cases, but single 3-D snapshots from the same type of motion with other side-edge conditions are shown at the far left in each row.

As noted previously, only steady single-hump shapes (purple) occur in two dimensions with fixed leading and trailing edges (Mavroyiakoumou & Alben 2020), whereas
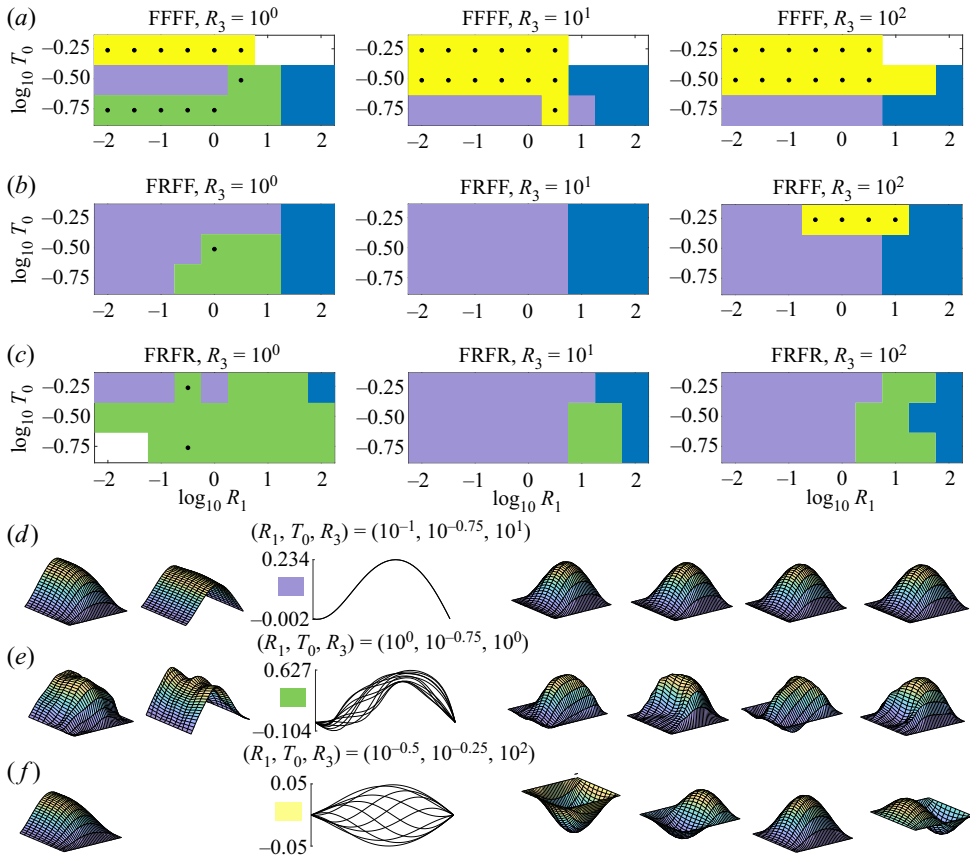
Figure 12. Typical membrane dynamics with fixed leading and trailing edges. The colour plots classify the different membrane dynamics across a grid of (R_1, T_0) values for three values of R_3 (10^0, 10^1, 10^2) with black dots indicating periodic motions. Recall that R_1 is the dimensionless membrane mass, T_0 is the dimensionless pretension and R_3 is the dimensionless stretching rigidity. Representative examples of motions in the purple, green and yellow regions are shown in $(d\text{--}f)$, identified by small coloured rectangles. To the right of the rectangles are overlaid sequences of 11 midspan snapshots in black, for FFFF boundary conditions. To the right of the midspan snapshots are a smaller representative sequence of four 3-D snapshots, from left to right with increasing time. To the left of the midspan snapshots are single 3-D snapshots representing similar cases with other side-edge conditions (FRFF and FRFR).

steady-state oscillations are surprisingly common in three dimensions, particularly with all four edges fixed. Here, up–down symmetric periodic motions (yellow) are much more common than with the other side-edge conditions, which typically have moderately small or no oscillations about a single-hump shape. The yellow motion includes a travelling wave of deflection that moves upstream, unlike in the 2-D fixed–free and free–free cases (Mavroyiakoumou & Alben 2020). Compared with the steady purple shape, the green motion has more variability not just in time but also in the spanwise direction, exemplified by the snapshot to the left of the small green rectangle in the second row from the bottom. In experiments, oscillatory cases with fixed leading and trailing edges have been reported mainly at non-zero angle of attack, where leading-edge vortex shedding seems particularly significant (Rojratsirikul, Wang & Gursul 2010, figure 4). Fewer details have been given for unsteady motions at zero angle of attack in experiments (Galvao *et al.* 2006).
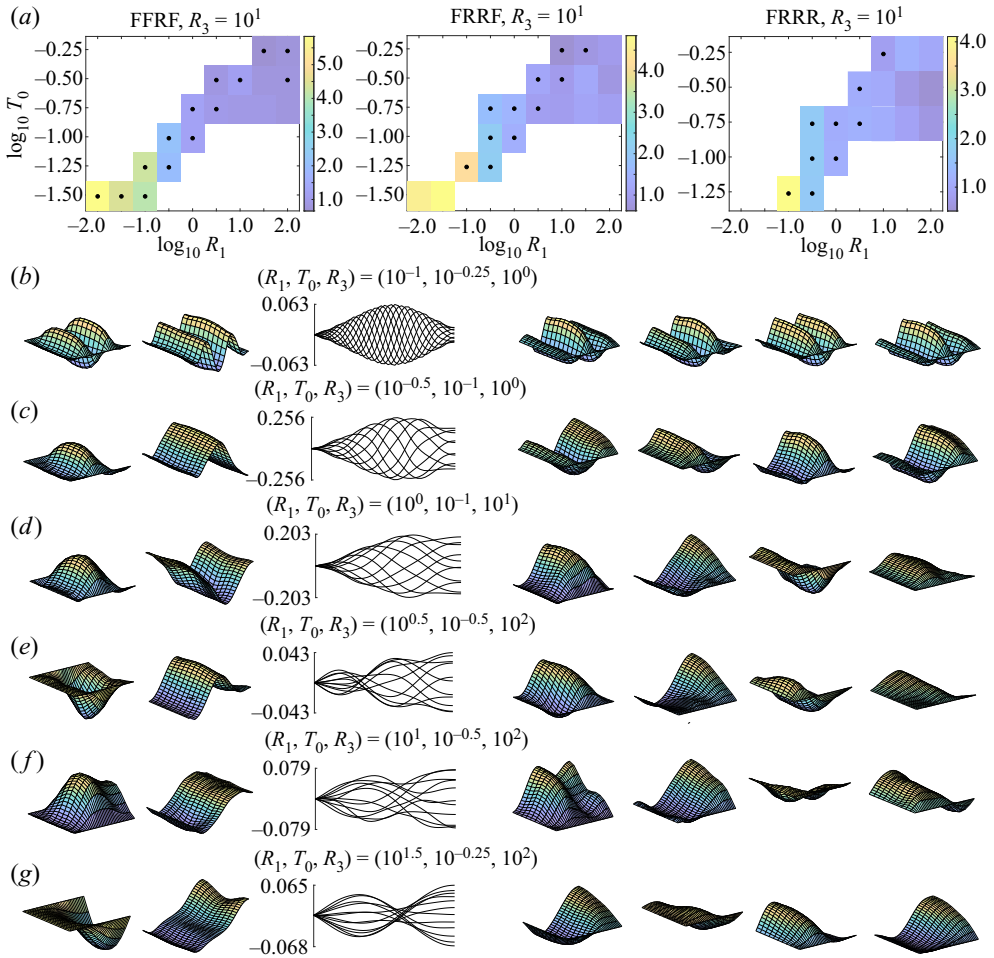
Figure 13. Typical membrane dynamics with fixed leading edges and free trailing edges. The colour plots in (*a*) show the time-averaged number of zero crossings of the membranes' midspan profiles at various (R_1, T_0) values for $R_3 = 10^1$. The black dots indicate periodic motions. Representative examples of motions at a sequence of R_1 values from 10^{-1} to $10^{1.5}$ are shown in (*b–g*). Overlaid sequences of 11 midspan snapshots are shown in black, for FRRF boundary conditions. To the right of the midspan snapshots are a smaller representative sequence of four 3-D snapshots, from left to right with increasing time. To the left of the midspan snapshots are single 3-D snapshots representing similar cases with other side-edge conditions (FFRF and FRRR).

5.2.2. *Leading edge fixed and trailing edge free (FFRF, FRRF, FRRR)*

The typical motions are qualitatively different in the second group (group 2 in figures 1 and 9), with the leading edge fixed and the trailing edge free. Hence, we classify the motions somewhat differently in figure 13, with colours denoting the number of times the midspan profile crosses $z = 0$ (not including the leading edge), time averaged. This classifies the spatial waviness of the profiles. Here, R_3 is fixed at 10^1; at other R_3 the deflection amplitude varies but the numbers of zero crossings are almost unchanged. The numbers of zero crossings decrease almost monotonically as R_1 increases, and chaotic states (without black dots) with larger amplitudes and more up–down asymmetry become more common, similarly to the 2-D results in Mavroyiakoumou & Alben (2020). In the

953 A32-28

white regions at the upper left of each panel, membranes are stable. In the white regions at the lower right, the computations did not converge when the membranes reached large amplitude but before they attained a steady-state motion, so results are not reported.

Typical membrane motions are shown in the rows at the bottom, one for each R_1 in a sequence from 10^{-1} to $10^{1.5}$. Here, the motions resemble different modes of a flapping flag (Connell & Yue 2007; Alben 2008b, 2022), with travelling waves that pass downstream, unlike for group 1. Another difference here is that the side-edge conditions do not change the type of motion. As in Mavroyiakoumou & Alben (2020), at small R_1 the deflection envelope has small amplitude near the trailing edge. At large R_1 (e.g. $10^{1.5}$) the travelling waves become more like standing waves, with fixed nodes and antinodes.

5.2.3. *Leading edge free and trailing edge fixed (RFFF, RRFF, RRFR)*

Next, we consider membranes whose leading edge is free and trailing edge is fixed (group 3 in figures 1 and 9). We showed in figure 9 that here the critical pretensions for instability are much larger than in the other cases. The space of motions is qualitatively different than for groups 1 and 2. In figure 14, we identify just three types of motions, with approximately periodic, up–down symmetric oscillations in most cases, characterized by three typical midspan profiles shown in the bottom three rows: a low-mode shape with at most a single interior z extremum (light purple), a higher-mode shape with one or two interior z extrema (yellow) and a low-mode shape with a multi-valued z profile near the trailing edge at certain times (dark purple). This last motion is more common at smaller R_1 and does not appear with both side edges fixed or at the largest R_3 (right column), where the first motion dominates. White regions are again cases in which the computations did not converge when the membranes reached large amplitude but before they attained a steady-state motion. Another special feature of group 3 is that the small-amplitude growth rates are generally much less than in the other groups, so data are omitted for $R_1 > 10^0$ because the amplitudes were growing and had not yet reached a steady state at $t = 350$. In some cases at $R_1 = 10^{1.5}$ and 10^2 (not shown) the amplitude neither grows nor decays noticeably after the initial perturbations, as also occurred in some 2-D cases at large R_1 (Mavroyiakoumou & Alben 2020).

The motions of group 3 seem more likely to violate the physical assumptions of the model than the other groups. The oscillation amplitude is highest at the leading edge, so leading-edge vortex shedding is probably important unless the oscillation amplitudes are very small (i.e. at $R_3 = 10^3$ and 10^4, where the motions are similar to those in the $R_3 = 10^2$ column, light purple generally). Vortex shedding would probably occur in multiple locations upstream of the trailing edge for the dark purple motions, due to large deflection amplitudes and slopes.

5.2.4. *Leading and trailing edges free (RFRF, RRRF, RRRR)*

Group 4 consists of membranes with the leading and trailing edges free (figures 1 and 9). With fewer of the edges fixed, we find a wider variety of dynamics. In figure 15 we use seven categories to classify the motions, with representative examples in the seven rows at the bottom, each labelled using a small rectangle with a certain colour and symbol that is repeated at data points in this category in the 3×3 array of colour plots above. The first three rows represent categories of steady shapes with one, two or three internal inflection points, respectively. The fourth row represents a category of motions with small oscillations about one of the steady shapes. To identify these cases, we decompose the midspan deflection $z(\alpha_1, 0, t)$ as the sum of its time average and the
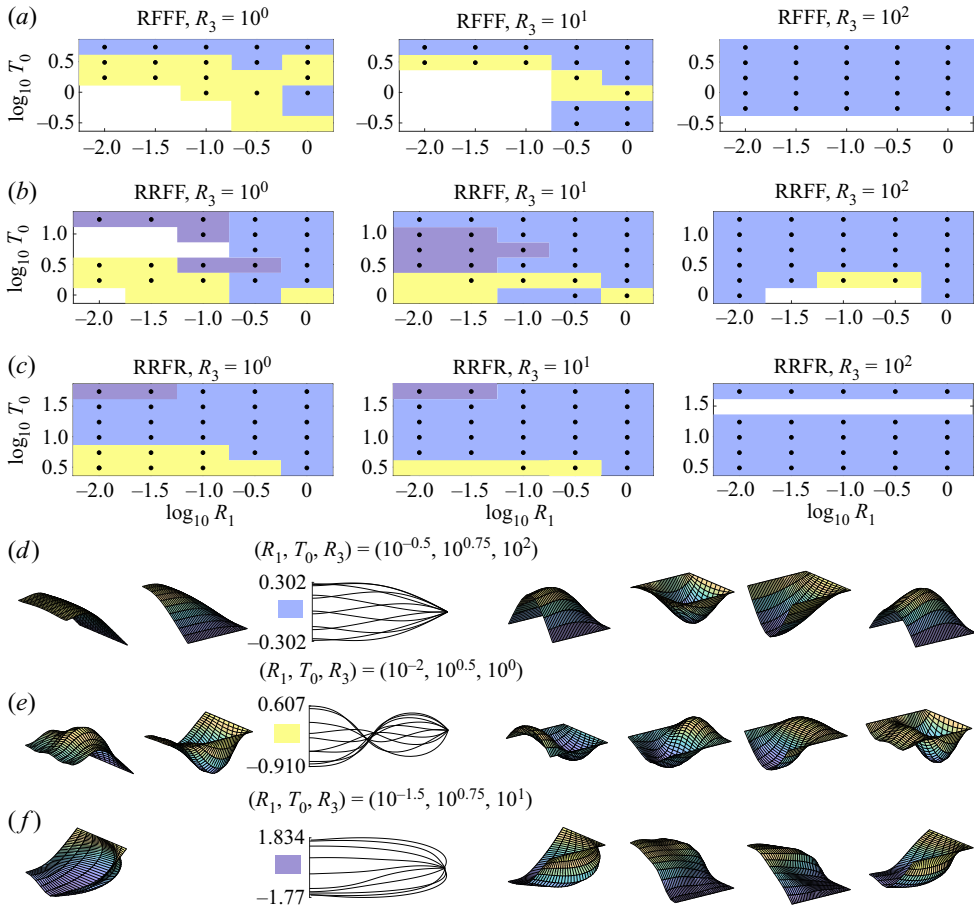
Figure 14. Typical membrane dynamics with free leading edges and fixed trailing edges. The colour plots classify the different membrane dynamics across a grid of (R_1, T_0) values for three values of R_3 (10^0, 10^1, 10^2) with black dots indicating periodic motions. Representative examples of motions in the light purple, yellow and dark purple regions are shown in (*d–f*), identified by small coloured rectangles. To the right of the rectangles are overlaid sequences of 11 midspan snapshots in black, for RFFF boundary conditions (*d,e*) and RRFF boundary conditions (*f*). To the right of the midspan snapshots are a smaller representative sequence of four 3-D snapshots, from left to right with increasing time. To the left of the midspan snapshots are single 3-D snapshots representing similar cases with other side-edge conditions (RRFR and RRFF).

remainder, the unsteady part. Motions are in the fourth category if the maximum minus the minimum of the unsteady deflection is non-zero but much less than the maximum minus the minimum of the time-averaged deflection. The fifth row represents unsteady motions whose unsteady part is comparable to or larger than the steady part (in the same sense as for the fourth category). The sixth row is for a special type of unsteady motion with all edges free (RRRR) that is time periodic. These motions have translational and deformational dynamics with $O(1)$ frequencies, and their translational motions are more precisely time periodic than those at large R_1. The seventh row is for another special type of unsteady RRRR motion that has both large spanwise and large chordwise curvatures.

The sixth and seventh categories occur only for the RRRR case, which seems to have a wider variety of motions because it is free to translate in z. As in the 2-D case (Mavroyiakoumou & Alben 2020), the translational motion is distinct from but coupled to
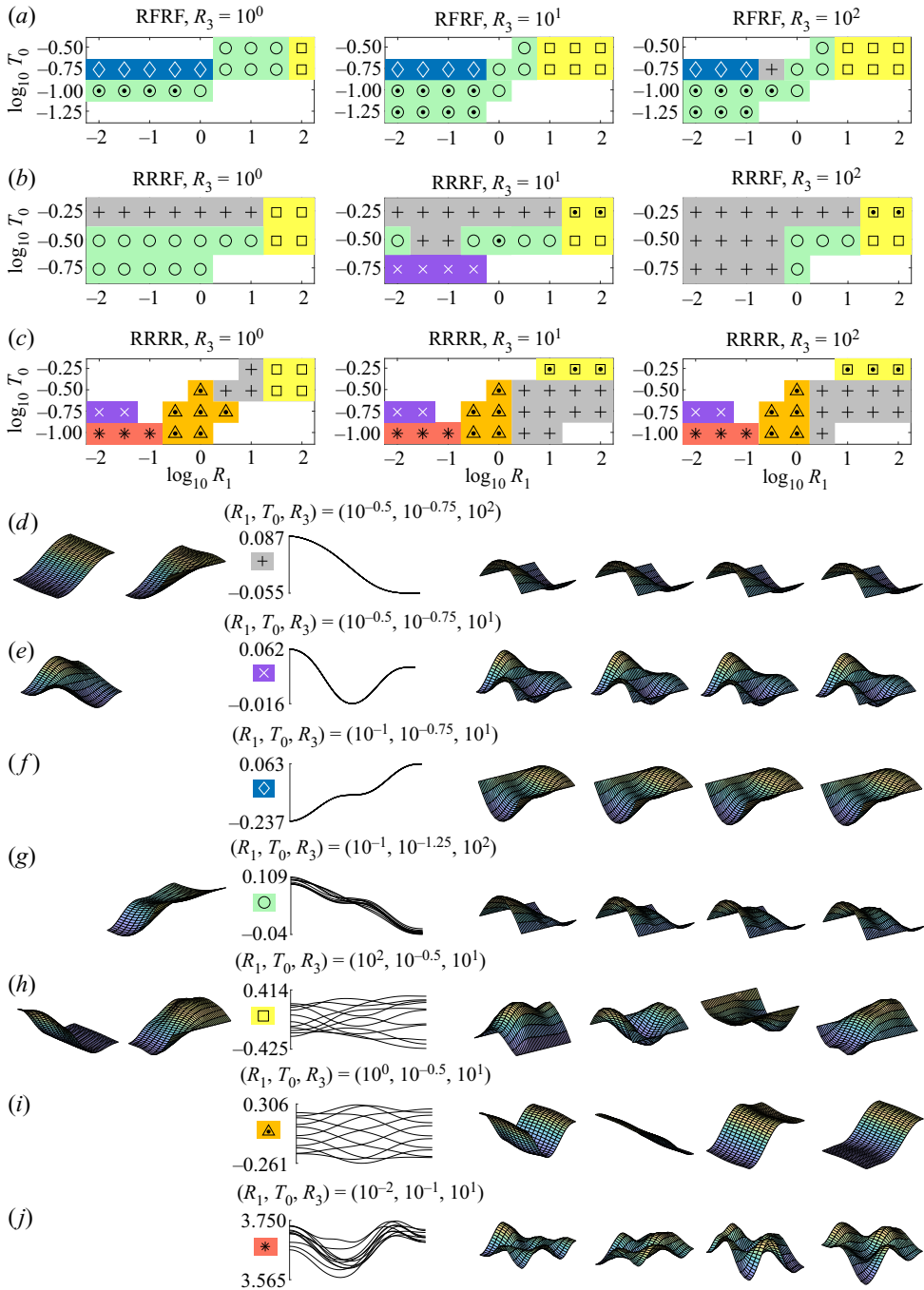
Figure 15. Typical membrane dynamics with free leading and trailing edges. The colour plots classify the different membrane dynamics across a grid of (R_1, T_0) values for three values of R_3 (10^0, 10^1, 10^2) with black dots indicating periodic motions. Representative examples of motions in all the coloured regions are shown in (*d–j*), identified by small coloured rectangles with symbols. To the right of the rectangles are overlaid sequences of 11 midspan snapshots in black, for RFRF (*d,f,g,h*), RRRF (*e*) and RRRR boundary conditions (*i,j*). To the right of the midspan snapshots are a smaller representative sequence of four 3-D snapshots, from left to right with increasing time. To the left of the midspan snapshots are single 3-D snapshots representing similar cases with other side-edge conditions (RRRF and RRRR).

the shape deformation dynamics, and the combination of the two results in more types of dynamics. Other categories of motions that occur only with certain edge conditions are the second and third, the steady states with two or three interior inflection points, respectively. The second occurs for RRRF and RRRR and the third for RFRF, both mainly at small R_1. The fourth category, small oscillations about a steady shape, occurs only with one or both side edges fixed (RFRF and RRRF). The first category, a steady shape with a single inflection point, occurs with all side edge conditions, but in the RRRR case it translates either up or down in z at almost constant speed, with occasional reversals in direction (as in Mavroyiakoumou & Alben 2020, figure 20). The fifth category, of general unsteady motions, occurs with all side-edge conditions at large R_1. Here, motions tend to be more asymmetrical and irregular and have larger oscillation amplitudes. The large body mass may allow the body to maintain its momentum against resisting fluid forces for longer times.

6. Conclusions

We have developed a model and numerical method to compute the small- and large-amplitude dynamics of thin membranes in 3-D inviscid flows. We provided numerical evidence that indicates convergence of our method with respect to spatial grid refinement. The 3-D solutions agree remarkably well with those computed in 2-D flows with different discretization techniques, particularly when the aspect ratio in three dimensions is large.

With fixed or free boundary conditions at each of the four edges, we have 16 combinations of boundary conditions for rectangular membranes, reduced to 12 when symmetric cases are accounted for. We computed the dynamics in all 12 cases with various values of the three key physical parameters: membrane mass (R_1), pretension (T_0) and stretching rigidity (R_3). The 12 cases fit naturally into four groups that are determined by the leading- and trailing-edge boundary conditions. Within each group there are strong similarities in the shapes and locations of the stability boundaries, the typical magnitudes of membranes' deflections and their oscillation frequencies in unsteady cases, and the typical shapes of the membranes at the midspan location. The side-edge boundary conditions can cause small or large qualitative differences in the dynamics within each group. The differences are relatively small for the fixed–free case (group 2); the midspan shape is almost unchanged at a free side edge or gradually scaled to flat at a fixed side edge. The differences are larger for the fixed–fixed and free–fixed cases (groups 1 and 3); changes in side-edge conditions lead to the appearance or disappearance of certain types of oscillation modes. In group 4 (free–free) the side edges have an even larger effect, for example by allowing or preventing translational motions that lead to a wider variety of dynamics.

As in two dimensions, the deflection magnitudes scale as $R_3^{-1/2}$ and the oscillation frequencies scale as $R_1^{-1/2}$ at large values of R_3 and R_1 respectively. The stability boundaries and dynamics in groups 1, 2 and 4 have many resemblances to the 2-D cases with same leading- and trailing-edge conditions studied in Mavroyiakoumou & Alben (2020). The fixed–free case in three dimensions is very similar to the 2-D case in terms of increasing waviness with decreasing R_1, a more limited effect of T_0 on the shapes and R_3 mainly setting the amplitudes of oscillation but not the shapes. The free–free case in three dimensions has some of the same types of states as in two dimensions: periodic oscillatory states and vertical translational states that may be nearly steady with a non-zero mean slope, or undergo periodic or chaotic oscillations.
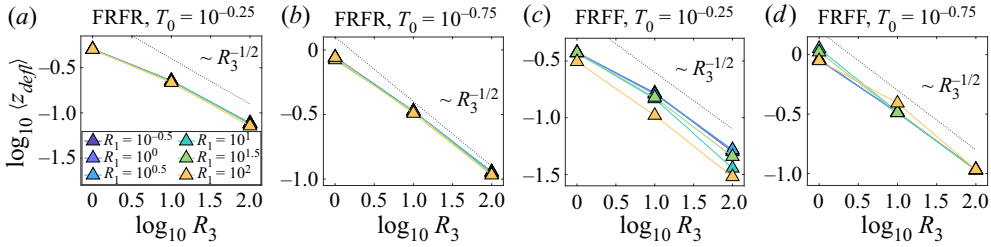
953 A32-32

Figure 16. Time-averaged deflections of FRFR and FRFF membranes (defined by (5.1)) vs R_3 for various R_1 and fixed T_0 ($10^{-0.25}$ and $10^{-0.75}$). The dotted black line indicates the scaling $R_3^{-1/2}$.

However, there are important qualitative differences in three dimensions. Unlike the 2-D fixed–fixed case where all membranes converge to steady single-hump shapes, the 3-D version (group 1) has cases with small and large unsteady oscillations, particularly when both side edges are fixed. The 3-D results contradicted our intuition from the 2-D study that more fixed edges lead to fewer unsteady states. The 3-D free–free case (group 4) has complicated spanwise curvature distributions, particularly with one or both side edges free. There are more types of motions here than in the 2-D free–free case. We did not study the 2-D analogue of group 3, free–fixed, but the variations with side-edge conditions here show that 3-D effects can be significant. Taken together these results validate the use of 2-D models for a good qualitative understanding of membrane motions and scaling with parameters, but also show that certain important phenomena can only be seen with the 3-D model.

Future work could investigate several topics, for example: the effect of aspect ratio; a non-zero Poisson ratio; including non-flat vortex sheets in the kinematic condition and computing wake roll-up (e.g. using a tree code Lindsay & Krasny 2001) and consequences for the membrane dynamics, especially at large mass density ratio and small stretching rigidity (Mavroyiakoumou & Alben 2020, figures 17 and 23); the types of motions at smaller T_0, which would require altering the algorithm to be able to compute steady-state motions in this regime; mixed fixed and free boundary conditions on a single edge; and different membrane shapes.

Author ORCIDs.
Christiana Mavroyiakoumou https://orcid.org/0000-0001-5828-6855;
Silas Alben https://orcid.org/0000-0002-8020-4999.

Appendix. Membrane deflections vs stretching rigidity at different pretension values

For two of the 12 boundary conditions (FRFF and FRFR) we plot in figure 16 the average membrane deflection at $T_0 = 10^{-0.25}$ and $10^{-0.75}$, instead of $10^{-0.5}$ in figure 10, and see that the deflection values increase at smaller T_0 (similarly to Mavroyiakoumou & Alben 2020; Tiomkin & Jaworski 2022) but the same $1/\sqrt{R_3}$ scaling holds in all cases.

REFERENCES

ABDULRAHIM, M., GARCIA, H. & LIND, R. 2005 Flight characteristics of shaping the membrane wing of a micro air vehicle. *J. Aircraft* **42** (1), 131–137.

ALBEN, S. 2008*a* Optimal flexibility of a flapping appendage in an inviscid fluid. *J. Fluid Mech.* **614**, 355–380.

ALBEN, S. 2008*b* The flapping-flag instability as a nonlinear eigenvalue problem. *Phys. Fluids* **20**, 104106.

ALBEN, S. 2009 Simulating the dynamics of flexible bodies and vortex sheets. *J. Comput. Phys.* **228** (7), 2587–2603.

ALBEN, S. 2010 Regularizing a vortex sheet near a separation point. *J. Comput. Phys.* **229** (13), 5280–5298.

ALBEN, S. 2022 Dynamics of flags over wide ranges of mass and bending stiffness. *Phys. Rev. Fluids* **7** (1), 013903.

ALBEN, S., GORODETSKY, A.A., KIM, D. & DEEGAN, R.D. 2019 Semi-implicit methods for the dynamics of elastic sheets. *J. Comput. Phys.* **399**, 108952.

ALBEN, S. & SHELLEY, M.J. 2008 Flapping states of a flag in an inviscid fluid: bistability and the transition to chaos. *Phys. Rev. Lett.* **100** (7), 074301.

ARBÓS-TORRENT, S., GANAPATHISUBRAMANI, B. & PALACIOS, R. 2013 Leading-and trailing-edge effects on the aeromechanics of membrane aerofoils. *J. Fluids Struct.* **38**, 107–126.

AYANCIK, F., FISH, F.E. & MOORED, K.W. 2020 Three-dimensional scaling laws of cetacean propulsion characterize the hydrodynamic interplay of flukes' shape and kinematics. *J. R. Soc. Interface* **17** (163), 20190655.

AYANCIK, F., MIVEHCHI, A. & MOORED, K.W. 2022 Scaling laws for three-dimensional combined heaving and pitching propulsors. *AIAA J.* **60** (5), 2930–2940.

BANERJEE, S., CONNELL, B.S.H. & YUE, D.K.P. 2015 Three-dimensional effects on flag flapping dynamics. *J. Fluid Mech.* **783**, 103–136.

BATCHELOR, G.K. 1967 *An Introduction to Fluid Dynamics*. Cambridge University Press.

BORAZJANI, I., GE, L., LE, T. & SOTIROPOULOS, F. 2013 A parallel overset-curvilinear-immersed boundary framework for simulating complex 3D incompressible flows. *Comput. Fluids* **77**, 76–96.

CHEN, Y., RYU, J., LIU, Y. & SUNG, H.J. 2020 Flapping dynamics of vertically clamped three-dimensional flexible flags in a poiseuille flow. *Phys. Fluids* **32** (7), 071905.

CHENEY, J.A., KONOW, N., BEARNOT, A. & SWARTZ, S.M. 2015 A wrinkle in flight: the role of elastin fibres in the mechanical behaviour of bat wing membranes. *J. R. Soc. Interface* **12** (106), 20141286.

COLE, J.A., MAUGHMER, M.D., BRAMESFELD, G., MELVILLE, M. & KINZEL, M. 2020 Unsteady lift prediction with a higher-order potential flow method. *Aerospace* **7** (5), 60.

COLGATE, S. 1996 *Fundamentals of Sailing, Cruising, and Racing*. WW Norton & Company.

CONNELL, B.S.H. & YUE, D.K.P. 2007 Flapping dynamics of a flag in a uniform stream. *J. Fluid Mech.* **581**, 33–67.

DAWOODIAN, M. & SAU, A. 2021 Kinetics and prey capture by a paddling jellyfish: three-dimensional simulation and lagrangian coherent structure analysis. *J. Fluid Mech.* **912**, A41.

DONG, D., CHEN, W. & SHI, S. 2016 Coupling motion and energy harvesting of two side-by-side flexible plates in a 3D uniform flow. *Appl. Sci.* **6** (5), 141.

EFRATI, E., SHARON, E. & KUPFERMAN, R. 2009 Elastic theory of unconstrained non-Euclidean plates. *J. Mech. Phys. Solids* **57** (4), 762–775.

ELOY, C., LAGRANGE, R., SOUILLIEZ, C. & SCHOUVEILER, L. 2008 Aeroelastic instability of cantilevered flexible plates in uniform flow. *J. Fluid Mech.* **611**, 97–106.

ELOY, C., SOUILLIEZ, C. & SCHOUVEILER, L. 2007 Flutter of a rectangular plate. *J. Fluids Struct.* **23**, 904–919.

FARLOW, S.J. 1993 *Partial Differential Equations for Scientists And Engineers*. Courier Corporation.

FENG, H. 2007 Vortex sheet simulations of 3D flows using an adaptive triangular panel/particle method. PhD thesis, University of Michigan.

FENG, H., KAGANOVSKIY, L. & KRASNY, R. 2009 Azimuthal instability of a vortex ring computed by a vortex sheet panel method. *Fluid Dyn. Res.* **41** (5), 051405.

FERNANDEZ-ESCUDERO, C., GAGNON, M., LAURENDEAU, E., PROTHIN, S., MICHON, G. & ROSS, A. 2019 Comparison of low, medium and high fidelity numerical methods for unsteady aerodynamics and nonlinear aeroelasticity. *J. Fluids Struct.* **91**, 102744.

FISH, F.E., SCHREIBER, C.M., MOORED, K.W., LIU, G., DONG, H. & BART-SMITH, H. 2016 Hydrodynamic performance of aquatic flapping: efficiency of underwater flight in the manta. *Aerospace* **3** (3), 20.

GALVAO, R., ISRAELI, E., SONG, A., TIAN, X., BISHOP, K., SWARTZ, S. & BREUER, K. 2006 The aerodynamics of compliant membrane wings modeled on mammalian flight mechanics. In *36th AIAA Fluid Dynamics Conference and Exhibit*. AIAA Paper 2006-2866.

GAZZOLA, M., ARGENTINA, M. & MAHADEVAN, L. 2014 Scaling macroscopic aquatic locomotion. *Nat. Phys.* **10** (10), 758–761.

GIBBS IV, S.C., WANG, I. & DOWELL, E.H. 2015 Stability of rectangular plates in subsonic flow with various boundary conditions. *J. Aircraft* **52** (2), 439–451.

GIBBS, S.C., WANG, I. & DOWELL, E. 2012 Theory and experiment for flutter of a rectangular plate with a fixed leading edge in three-dimensional axial flow. *J. Fluids Struct.* **34**, 68–83.

GOLBERG, M.A. 1990 *Numerical Solution of Integral Equations*. Plenum Press.

GRAFF, K.F. 1975 *Wave Motion in Elastic Solids*. Oxford University Press.

GROZDANOV, A. 2017 *Transonic Static Aeroelasticity Using the 2.5D Nonlinear Vortex Lattice Method*. École Polytechnique.

HESS, J.L. & SMITH, A.M.O. 1967 Calculation of potential flow about arbitrary bodies. *Prog. Aerosp. Sci.* **8**, 1–138.

HIROAKI, K., HAYASHI, Y. & WATANABE, M. 2021 Numerical simulation on a limit cycle oscillation of a rectangular sheet in three-dimensional flow: influence of vortex element model on post-critical behavior. *Nonlinear Dyn.* **106** (4), 2893–2917.

HIROAKI, K. & WATANABE, M. 2021*a* Theoretical study on the instability mechanism of flutter generated on a cantilevered flexible plate in three-dimensional uniform flow. *Acta Mech.* **232** (7), 2897–2917.

HIROAKI, K. & WATANABE, M. 2021*b* Three-dimensional nonlinear analysis and wind-tunnel experiment of flutter generated on a rectangular sheet in uniform flow. *J. Fluids Struct.* **101**, 103226.

HOOVER, A.P., GRIFFITH, B.E. & MILLER, L.A. 2017 Quantifying performance in the medusan mechanospace with an actively swimming three-dimensional jellyfish model. *J. Fluid Mech.* **813**, 1112–1155.

HOOVER, A.P. & TYTELL, E. 2020 Decoding the relationships between body shape, tail beat frequency, and stability for swimming fish. *Fluids* **5** (4), 215.

HOOVER, A.P., XU, N.W., GEMMELL, B.J., COLIN, S.P., COSTELLO, J.H., DABIRI, J.O. & MILLER, L.A. 2021 Neuromechanical wave resonance in jellyfish swimming. *Proc. Natl Acad. Sci.* **118** (11), e2020025118.

HOUGH, G.R. 1973 Remarks on vortex-lattice methods. *J. Aircraft* **10** (5), 314–317.

HU, H., TAMAI, M. & MURPHY, J.T. 2008 Flexible-membrane airfoils at low Reynolds numbers. *J. Aircraft* **45** (5), 1767–1778.

HUANG, W.X. & SUNG, H.J. 2010 Three-dimensional simulation of a flapping flag in a uniform flow. *J. Fluid Mech.* **653**, 301–336.

IZRAELEVITZ, J.S., ZHU, Q. & TRIANTAFYLLOU, M.S. 2017 State-space adaptation of unsteady lifting line theory: twisting/flapping wings of finite span. *AIAA J.* **55** (4), 1279–1294.

JAMES, R.M. 1972 On the remarkable accuracy of the vortex lattice method. *Comput. Meth. Appl. Mech. Engng* **1** (1), 59–79.

JAWORSKI, J.W. & GORDNIER, R.E. 2012 High-order simulations of low Reynolds number membrane airfoils under prescribed motion. *J. Fluids Struct.* **31**, 49–66.

KAGANOVSKIY, L. 2006 Adaptive panel method for particle simulation of three dimensional vortex sheet motion. PhD thesis, University of Michigan.

KAGEMOTO, H., WOLFGANG, M.J., YUE, D.K.P. & TRIANTAFYLLOU, M.S. 2000 Force and power estimation in fish-like locomotion using a vortex-lattice method. *Trans. ASME J. Fluids Engng* **122** (2), 239–253.

KATZ, J. & PLOTKIN, A. 2001 *Low-Speed Aerodynamics*, vol. 13. Cambridge University Press.

KIM, Y. & PESKIN, C.S. 2007 Penalty immersed boundary method for an elastic boundary with mass. *Phys. Fluids* **19** (5), 053103.

KIMBALL, J. 2009 *Physics of Sailing*. CRC Press.

LABARBE, J. & KIRILLOV, O.N. 2020 Membrane flutter induced by radiation of surface gravity waves on a uniform flow. *J. Fluid Mech.* **901**, A4.

LABARBE, J. & KIRILLOV, O.N. 2022 Radiation-induced instability of a finite-chord Nemtsov membrane. *Phys. Fluids* **34** (1), 014106.

LAUDER, G.V., ANDERSON, E.J., TANGORRA, J. & MADDEN, P.G.A. 2007 Fish biorobotics: kinematics and hydrodynamics of self-propulsion. *J. Expl Biol.* **210** (16), 2767–2780.

LE MAÎTRE, O., HUBERSON, S. & DE CURSI, E.S. 1999 Unsteady model of sail and flow interaction. *J. Fluids Struct.* **13** (1), 37–59.

LI, T., *et al.* 2017 Fast-moving soft electronic fish. *Sci. Adv.* **3** (4), e1602045.

LI, G., JAIMAN, R.K. & KHOO, B.C. 2021 Flow-excited membrane instability at moderate Reynolds numbers. *J. Fluid Mech.* **929**, A40.

LI, G., JAIMAN, R.K. & KHOO, B.C. 2022 Aeroelastic mode decomposition framework and mode selection mechanism in fluid–membrane interaction. *J. Fluids Struct.* **108**, 103428.

LI, G., LAW, Y.Z. & JAIMAN, R.K. 2019 A novel 3D variational aeroelastic framework for flexible multibody dynamics: application to bat-like flapping dynamics. *Comput. Fluids* **180**, 96–116.

LIAN, Y. & SHYY, W. 2005 Numerical simulations of membrane wing aerodynamics for micro air vehicle applications. *J. Aircraft* **42** (4), 865–873.

LIAN, Y., SHYY, W., VIIERU, D. & ZHANG, B. 2003 Membrane wing aerodynamics for micro air vehicles. *Prog. Aerosp. Sci.* **39** (6–7), 425–465.

LIAO, J.C., BEAL, D.N., LAUDER, G.V. & TRIANTAFYLLOU, M.S. 2003 Fish exploiting vortices decrease muscle activity. *Science* **302** (5650), 1566–1569.

LINDSAY, K. & KRASNY, R. 2001 A particle method and adaptive treecode for vortex sheet motion in three-dimensional flow. *J. Comput. Phys.* **172** (2), 879–907.

LIU, P. 1996 A time-domain panel method for oscillating propulsors with both chordwise and spanwise flexibility. PhD thesis, Memorial University of Newfoundland.

LIU, P. & BOSE, N. 1997 Propulsive performance from oscillating propulsors with spanwise flexibility. *Proc. R. Soc. Lond.* A **453** (1963), 1763–1770.

LONG, L.N. & FRITZ, T.E. 2004 Object-oriented unsteady vortex lattice method for flapping flight. *J. Aircraft* **41** (6), 1275–1290.

MARGASON, R., KJELGAARD, S., SELLERS, W. III, Morris, C. JR., WALKEY, K. & SHIELDS, E. 1985 Subsonic panel methods-a comparison of several production codes. In *23rd Aerospace Sciences Meeting*. *AIAA Paper* 1985-280.

MASOUD, H. & ALEXEEV, A. 2010 Resonance of flexible flapping wings at low Reynolds number. *Phys. Rev. E* **81** (5), 056304.

MAVROYIAKOUMOU, C. & ALBEN, S. 2020 Large-amplitude membrane flutter in inviscid flow. *J. Fluid Mech.* **891**, A23.

MAVROYIAKOUMOU, C. & ALBEN, S. 2021*a* Dynamics of tethered membranes in inviscid flow. *J. Fluids Struct.* **107**, 103384.

MAVROYIAKOUMOU, C. & ALBEN, S. 2021*b* Eigenmode analysis of membrane stability in inviscid flow. *Phys. Rev. Fluids* **6**, 043901.

MICHELIN, S. & LLEWELLYN SMITH, S.G. 2009 Resonance and propulsion performance of a heaving flexible wing. *Phys. Fluids* **21** (7), 071902.

MITTAL, R., DONG, H., BOZKURTTAS, M., NAJJAR, F.M., VARGAS, A. & VON LOEBBECKE, A. 2008 A versatile sharp interface immersed boundary method for incompressible flows with complex boundaries. *J. Comput. Phys.* **227** (10), 4825–4852.

MOORED, K.W. 2018 Unsteady three-dimensional boundary element method for self-propelled bio-inspired locomotion. *Comput. Fluids* **167**, 324–340.

MOUGEL, J. & MICHELIN, S. 2020 Flutter and resonances of a flag near a free surface. *J. Fluids Struct.* **96**, 103046.

MURUA, J., PALACIOS, R. & GRAHAM, J.M.R. 2012 Applications of the unsteady vortex-lattice method in aircraft aeroelasticity and flight dynamics. *Prog. Aerosp. Sci.* **55**, 46–72.

NARDINI, M., ILLINGWORTH, S.J. & SANDBERG, R.D. 2018 Reduced-order modeling for fluid-structure interaction of membrane wings at low and moderate Reynolds numbers. In *2018 AIAA Aerospace Sciences Meeting*. *AIAA Paper* 2018-1544.

NGUYEN, A.T., KIM, J.-K., HAN, J.-S. & HAN, J.-H. 2016 Extended unsteady vortex-lattice method for insect flapping wings. *J. Aircraft* **53** (6), 1709–1718.

PAN, Y., DONG, X., ZHU, Q. & YUE, D.K.P. 2012 Boundary-element method for the prediction of performance of flapping foils with leading-edge separation. *J. Fluid Mech.* **698**, 446–467.

PEPPER, W.B. & MAYDEW, R.C. 1971 Aerodynamic decelerators-an engineering review. *J. Aircraft* **8** (1), 3–19.

PIQUEE, J., LÓPEZ, I., BREITSAMTER, C., WÜCHNER, R. & BLETZINGER, K.-U. 2018 Aerodynamic characteristics of an elasto-flexible membrane wing based on experimental and numerical investigations. In *2018 Applied Aerodynamics Conference*. *AIAA Paper* 2018-3338.

RALSTON, A. & RABINOWITZ, P. 2001 *A First Course in Numerical Analysis*. Courier Corporation.

RAMESH, K., GOPALARATHNAM, A., GRANLUND, K., OL, M.V. & EDWARDS, J.R. 2014 Discrete-vortex method with novel shedding criterion for unsteady aerofoil flows with intermittent leading-edge vortex shedding. *J. Fluid Mech.* **751**, 500–538.

Membrane flutter in three-dimensional inviscid flow

ROJRATSIRIKUL, P., WANG, Z. & GURSUL, I. 2010 Unsteady fluid-structure interactions of membrane airfoils at low Reynolds numbers. In *Animal Locomotion* (ed. G.K. Taylor, M.S. Triantafyllou & C. Tropea), pp. 297–310. Springer.

RUS, D. & TOLLEY, M.T. 2015 Design, fabrication and control of soft robots. *Nature* **521** (7553), 467–475.

SAFFMAN, P.G. 1992 *Vortex Dynamics*. Cambridge University Press.

SAKAJO, T. 2001 Numerical computation of a three-dimensional vortex sheet in a swirl flow. *Fluid Dyn. Res.* **28** (6), 423–448.

SCHOMBERG, T., GERLAND, F., LIESE, F., WÜNSCH, O. & RUETTEN, M. 2018 Transition manipulation by the use of an electrorheologically driven membrane. In *2018 Flow Control Conference*. *AIAA Paper* 2018-3213.

SHUKLA, R.K. & ELDREDGE, J.D. 2007 An inviscid model for vortex shedding from a deforming body. *Theor. Comput. Fluid Dyn.* **21** (5), 343.

SHYY, W., BERG, M. & LJUNGQVIST, D. 1999 Flapping and flexible wings for biological and micro air vehicles. *Prog. Aerosp. Sci.* **35** (5), 455–505.

SONG, A., TIAN, X., ISRAELI, E., GALVAO, R., BISHOP, K., SWARTZ, S. & BREUER, K. 2008 Aeromechanics of membrane wings with implications for animal flight. *AIAA J.* **46** (8), 2096.

STANFORD, B., IFJU, P., ALBERTANI, R. & SHYY, W. 2008 Fixed membrane wings for micro air vehicles: experimental characterization, numerical modeling, and tailoring. *Prog. Aerosp. Sci.* **44** (4), 258–294.

STEIN, K., BENNEY, R., KALRO, V., TEZDUYAR, T.E., LEONARD, J. & ACCORSI, M. 2000 Parachute fluid–structure interactions: 3-D computation. *Comput. Meth. Appl. Mech. Engng* **190** (3–4), 373–386.

SUNNY, M.R., SULTAN, C. & KAPANIA, R.K. 2014 Optimal energy harvesting from a membrane attached to a tensegrity structure. *AIAA J.* **52** (2), 307–319.

SWARTZ, S.M., GROVES, M.S., KIM, H.D. & WALSH, W.R. 1996 Mechanical properties of bat wing membrane skin. *J. Zool.* **239** (2), 357–378.

SWARTZ, S., IRIARTE-DIAZ, J., RISKIN, D., TIAN, X., SONG, A. & BREUER, K. 2007 Wing structure and the aerodynamic basis of flight in bats. In *45th AIAA Aerospace Sciences Meeting and Exhibit*. *AIAA Paper* 2007-42.

SYGULSKI, R. 2007 Stability of membrane in low subsonic flow. *Intl J. Non-Linear Mech.* **42** (1), 196–202.

TANG, D. & DOWELL, E.H. 2001 Effects of angle of attack on nonlinear flutter of a delta wing. *AIAA J.* **39** (1), 15–21.

TANG, D., DOWELL, E.H. & HALL, K.C. 1999 Limit cycle oscillations of a cantilevered wing in low subsonic flow. *AIAA J.* **37** (3), 364–371.

TANG, C., HUANG, H., GAO, P. & LU, X.-Y. 2016 Self-propulsion of a flapping flexible plate near the ground. *Phys. Rev.* E **94** (3), 033113.

TIAN, F., LU, X. & LUO, H. 2012 Onset of instability of a flag in uniform flow. *Theor. Appl. Mech. Lett.* **2** (2), 022005.

TIOMKIN, S. & JAWORSKI, J.W. 2022 Unsteady aerodynamic theory for membrane wings. *J. Fluid Mech.* **948**, A33.

TIOMKIN, S. & RAVEH, D.E. 2017 On the stability of two-dimensional membrane wings. *J. Fluids Struct.* **71**, 143–163.

TIOMKIN, S. & RAVEH, D.E. 2021 A review of membrane-wing aeroelasticity. *Prog. Aerosp. Sci.* **126**, 100738.

TRIANTAFYLLOU, M.S. & HOWELL, C.T. 1994 Dynamic response of cables under negative tension: an ill-posed problem. *J. Sound Vib.* **173** (4), 433–447.

TRIANTAFYLLOU, M.S., TRIANTAFYLLOU, G.S. & YUE, D.K.P. 2000 Hydrodynamics of fishlike swimming. *Annu. Rev. Fluid Mech.* **32** (1), 33–53.

TZEZANA, G.A. & BREUER, K.S. 2019 Thrust, drag and wake structure in flapping compliant membrane wings. *J. Fluid Mech.* **862**, 871–888.

WILLIS, D.J., ISRAELI, E., PERSSON, P.-O., DRELA, M., PERAIRE, J., SWARTZ, S. & BREUER, K. 2007*a* A computational framework for fluid structure interaction in biologically inspired flapping flight. In *25th AIAA Applied Aerodynamics Conference*, p. 3803.

WILLIS, D.J., PERAIRE, J. & WHITE, J.K. 2006 A quadratic basis function, quadratic geometry, high order panel method. In *44th AIAA Aerospace Sciences Meeting and Exhibit*. *AIAA Paper* 2006-1253.

WILLIS, D.J., PERAIRE, J. & WHITE, J.K. 2007*b* A combined pFFT-multipole tree code, unsteady panel method with vortex particle wakes. *Intl J. Numer. Meth. Fluids* **53** (8), 1399–1422.

WILLIS, D.J. & PERSSON, P.-O. 2014 Multiple-fidelity computational framework for the design of efficient flapping wings. *AIAA J.* **52** (12), 2840–2854.

YANG, S. & SULTAN, C. 2016 Modeling of tensegrity-membrane systems. *Intl J. Solids Struct.* **82**, 125–143.

YEH, D.T. & PLOTKIN, A. 1986 Vortex panel calculation of wake rollup behind a large aspect ratio wing. *AIAA J.* **24** (9), 1417–1423.

YU, Z., WANG, Y. & SHAO, X. 2012 Numerical simulations of the flapping of a three-dimensional flexible plate in uniform flow. *J. Sound Vib.* **331** (20), 4448–4463.

ZHU, L., HE, G., WANG, S., MILLER, L., ZHANG, X., YOU, Q. & FANG, S. 2011 An immersed boundary method based on the lattice Boltzmann approach in three dimensions, with application. *Comput. Maths Applics.* **61** (12), 3506–3518.

ZHU, Q., WOLFGANG, M.J., YUE, D.K.P. & TRIANTAFYLLOU, M.S. 2002 Three-dimensional flow structures and vorticity control in fish-like swimming. *J. Fluid Mech.* **468**, 1–28.